

NELIOTA: New results and updated statistics after 6.5 years of lunar impact flashes monitoring

A. Liakos¹, A. Z. Bonanos¹, E. M. Xilouris¹, D. Koschny²,
I. Bellas-Velidis¹, P. Boumis¹, A. Maroussis¹, and R. Moissl³

¹ Institute for Astronomy, Astrophysics, Space Applications and Remote Sensing, National Observatory of Athens, Metaxa & Vas. Pavlou St., GR-15236, Penteli, Athens, Greece
e-mail: alliakos@noa.gr

² Lunar and Planetary Exploration, Technical University of Munich, 85521 Ottobrunn, Germany

³ Near Earth Object Coordination Centre, European Space Research Institute (ESA/ESRIN), Largo Galileo Galilei 1, 00044 Frascati (Roma), Italy

Received XX January 2024; accepted XX January 2024

ABSTRACT

We present results of the NELIOTA campaign for lunar impact flashes observed with the 1.2 m Kryoneri telescope. From August 2019 to August 2023, we report 113 validated and 70 suspected flashes. For the validated flashes, we calculate the physical parameters (masses, radii) of the corresponding projectiles, the temperatures developed during the impacts, and the expected crater sizes. For the multiframe flashes we present light curves and thermal evolution plots. Using the whole sample of NELIOTA that encompasses 192 validated flashes in total from 2017, the statistics of the physical parameters of the meteoroids, the peak temperatures of the impacts and the expected crater sizes has been updated. Using this large sample, empirical relations correlating the luminous energies per photometric band were derived and used to roughly estimate the parameters of 92 suspected flashes of the NELIOTA archive. For a typical value of the luminous efficiency, we found that the majority ($> 75\%$) of the impacting meteoroids have masses between 1–200 g, radii between 0.5–3 cm and produced craters up to 3.5 m. 85% of the peak temperatures of the impacts range between 2000 and 4500 K. Statistics regarding the magnitude decline and the cooling rates of the multiframe flashes are also presented. The recalculation of the appearance frequency of meteoroids, lying within the aforementioned ranges of physical parameters, on the Moon yields that the total lunar surface is bombarded with 7.4 sporadic meteoroids per hour and up to 12.6 meteoroids per hour when the Earth-Moon system passes through a strong meteoroid stream. By extrapolating these rates on Earth, the respective rates for various distances from its surface are calculated and used to estimate the probability of an impact of a meteoroid with a hypothetical infrastructure on the Moon, or with a satellite orbiting Earth for various impact surfaces and duration times of the missions.

Key words. Meteorites, meteors, meteoroids – Moon – Techniques: photometric

1. Introduction

The increasing number of artificial satellites and space missions, especially during the last decade and the following few years, increased the interest for the study of meteoroids, since the probability of an impact with a space vehicle is not negligible anymore (e.g., the micrometeoroid impact on JWST six months after its launch). In addition, during the last decade, space agencies focussed more and more on the construction of bases on Moon (e.g., the NASA-Artemis mission) and, later, on other planets (e.g., Mars). Due to the lack of atmosphere in the aforementioned ‘targets’, meteoroids may hit directly the established infrastructure and cause serious damage. Therefore, the space vehicle designers and the civil engineers should be aware of the appearance frequency of these objects as well as of their affect on infrastructure (i.e., due to the impact or the increased temperature) in order to calculate the probability of being hit and establish appropriate mitigation measures.

Lunar impact flashes (hereafter LIFs) have been studied for more than 25 years and they are caused by the larger meteoroids of cm–to–dm sizes. These object sizes can be considered as the most dangerous and they are those that produce observable LIFs from the Earth. On the contrary, the majority of the meteors ob-

served on Earth are produced by smaller size meteoroids and only those that produce bolide or fireball events can be compared in size with those that produce the observed LIFs. Fireballs and bolides are rarely observed from a given site (i.e., the sky coverage is approximately 6×10^4 km²) and large networks are needed for their detection. Meteors follow different physics (i.e., evaporation due to the atmospheric friction) than that of LIFs and can provide us with important information, such as velocities, origin, meteorite remnants. The Moon, however, is used as an extremely large impact surface (i.e., the near side of the Moon is 1.9×10^7 km²) for studying the impacts of larger size meteoroids and asteroids. Observations of LIFs are very important as they can provide the size frequency distribution of meteoroids and also directly affect space industry.

In the absence of an atmosphere on the Moon, meteoroids directly impact its surface. Their kinetic energy is converted to: a) heating the impacted material, b) kinetic energy of the ejecta, and c) crater excavation. The heating of the material produces light emission (i.e., luminous energy LE), which generates the so-called impact flash. According to the results of Liakos et al. (2020), the peak temperatures of the flashes vary between 1500–6000 K, while their thermal evolution in time, in general, shows rapid decrease (see also Bouley et al. 2012). The majority of the

flashes last less than 66 ms and they mostly emit in the near-infrared passbands (Liakos et al. 2020).

One of the major open questions in the study of LIFs concerns the luminous efficiency η of the LIFs that is the fraction of the luminous over the kinetic energy. Using data from LIFs observed during meteoroid streams (i.e., known velocities of the projectiles from the respective meteor showers on Earth), many research teams (Bellot Rubio et al. 2000a,b; Ortiz et al. 2006; Moser et al. 2011; Swift et al. 2011; Bouley et al. 2012; Suggs et al. 2014; Madiedo et al. 2015b, 2017, 2018, 2019) have resulted in values between $5 \times 10^{-4} < \eta < 5 \times 10^{-3}$. The NELIOTA team, using dualband observations, determined that η is wavelength dependent and found correlations between η per band ratio and the peak temperature of the flash (Liakos et al. 2020).

The ‘Near-Earth objects Lunar Impacts and Optical Transients’ (NELIOTA¹) project began in 2015 at the National Observatory of Athens (NOA) and was funded by the European Space Agency (ESA). The observations began on February 2017 and officially ended in mid-August 2023. The NELIOTA team has published so far three papers in peer-reviewed journals, namely, Bonanos et al. (2018, hereafter Paper I), Xilouris et al. (2018, hereafter Paper II), Liakos et al. (2020, hereafter Paper III), while other research works were also based on the NELIOTA data (Avdellidou & Vaubaillon 2019; Munaibari et al. 2020; Avdellidou et al. 2021).

In this paper, we present the detailed results for the LIFs observed from NELIOTA after July 2019 following the same methods described in Paper III. Section 2 briefly describes the observational strategy, the followed validation procedure, and the observations efficiency statistics of the programme. Section 3 hosts the catalog of the observed LIFs during the aforementioned time-period that includes their photometric measurements and coordinates. The physical characteristics of the meteoroids produced these LIFs, the peak temperatures of the impacts and the expected crater sizes are given in Section 4. Additionally, in this section, using all the available data from the inception of NELIOTA, statistics for the physical properties of these objects and the impacts are also presented. Updated correlations between the properties of meteoroids and LIFs are given in Section 5. In Section 6, using the whole sample of NELIOTA, we derive the detection rate of LIFs and calculate the appearance frequency of the meteoroids on Moon and, by extrapolation, in the vicinity of the Earth. Moreover, we calculate the meteoroid impact probability with a potential lunar infrastructure and with an orbiting satellite. Section 7 contains a discussion about the observations, results, and the future studies of LIFs, based on our experience, while Section 8 contains a summary of the current results and concluding remarks.

2. Observations and efficiency statistics of the campaign

The long-term monitoring of the Moon for LIFs utilized the 1.2 m Kryoneri telescope² (prime focus optical design, f/2.8) and a twin fast-frame camera system installed on a dichroic beam splitter (see Paper II for details). We observe the nightside of the Moon in the *R* and *I* passbands simultaneously (with a synchronization accuracy of 6 ms) with a frame rate of 30 fps. The exposure time of the cameras is 23 ms followed by a readout time of 10 ms. Our set-up has an angular Field-of-View (FoV)

of $16' \times 14.4'$ and covers a mean lunar surface of 3×10^6 km². The Moon is observed during approximately the illumination phases 0.1 ± 0.01 and 0.45 ± 0.01 depending on the Earth-Moon distance. The observations are divided into 15 min lunar chunks separated by standard stars observations chunks. The telescope, cameras and the rest subsystems are controlled by a custom developed software (NELIOTA-OBS), which is also used for the observation planning and the data storing.

The data are reduced with a second custom developed software (NELIOTA-DET), which detects the potential events in the difference images. The validation is based on visual inspection by an expert user and follows strictly the NELIOTA validation flowchart (Paper III/ Fig. 3 and Liakos et al. 2019). Briefly, detections in both cameras that do not appear as moving in successive frames are characterized as validated LIFs. Multi- or single-frame detections (with similar photometric profiles, i.e., images, with the standard stars) in *I* passband only are characterized as suspected LIFs of class 1 (SC1) and 2 (SC2), respectively.

We assume that false detections coming from satellite glints shorter than our exposure time are so rare that they are negligible. For this, we have checked all validated and suspected flashes against two publicly available databases, one from space-track.org³ and the other one by Bill Gray⁴. We checked all event times for possible satellites within 0.25 degrees to the Moon center. For the validated events, this is the case in 14% of the cases. We assume that about 90% of all satellites are in orbits low enough that they should have been recognised by their movement, even during a short light reflection on one of their surfaces. This leads to a very first rough estimate for a false detection percentage of $0.14 * (1 - 0.9) < 1.4\%$. Only a small percentage of these will show a glint that can be mistaken for an impact flash, further reducing the probability of this to happen. For the rest of the paper, we thus neglect any satellite contamination. A more detailed estimate of any false detections is beyond the scope of this paper.

Aperture photometry is used for the photon flux calculation per band for the validated and suspected LIFs based on the standard star observations. Using highly detailed maps of the Moon (taken from the Virtual Moon Atlas Software⁵) and the localization tool of the NELIOTA-DET software, we estimate the selenographic coordinates of the LIFs with an error of 0.5° . The data of the validated and suspected LIFs are, subsequently, uploaded into the project’s website⁶ within 24 hours of observations, by employing another custom developed software (NELIOTA-ARC), and made publicly available.

The observational statistics regarding the observed hours, number of detections and efficiency of the campaign for the period August 2019 - mid August 2023 are plotted in Fig. 1. The total available time for this time period was approximately 679 h. It should be noticed that approximately 35-40% of this available time is a-priori lost due to the readout time of the cameras (30%) and the standard stars observations (5-10%), cf. Paper III. Therefore, the true available time on Moon was actually 429.56 h. From this true available time, the Moon was observed for a total of 172.9 h (40.3%) (see Fig. 1-upper and middle panels), while 217.2 h (50.6%) and 39.5 h (9.1%) were lost due to bad weather conditions and technical issues, respectively (see Fig. 1-upper panel). Within this time period, 113 validated and 70 suspected flashes were detected (see Fig. 1-lower panel). The respective

³ <https://www.space-track.org>

⁴ <https://www.github.com/BillGray/Tles/>

⁵ <https://ap-i.net/avl/en/start>

⁶ <https://neliota.astro.noa.gr/DataAccess>

¹ <https://neliota.astro.noa.gr/>

² <https://kryoneri.astro.noa.gr/en/>

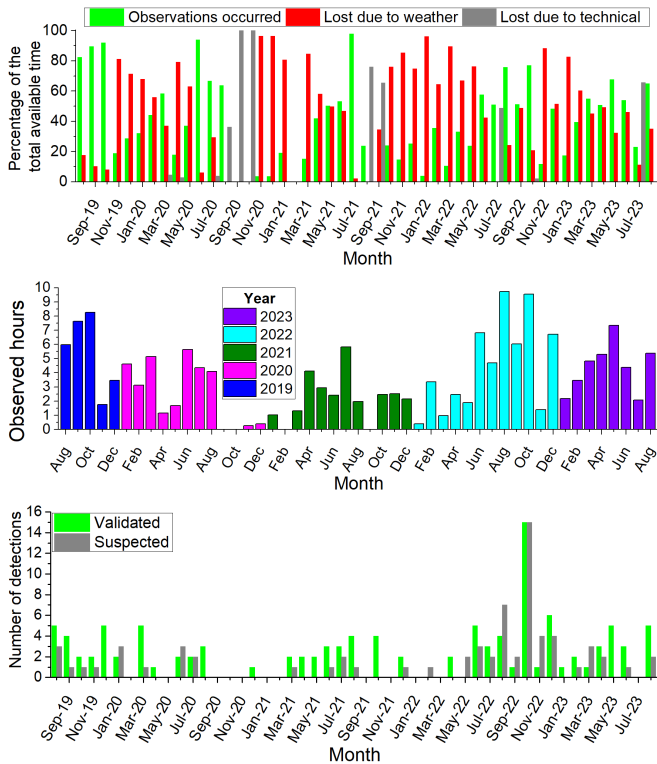


Fig. 1: Observational statistics of the NELIOTA campaign between August 2019 and mid-August 2023. The upper plot shows the percentages of: a) the observed time, b) the time lost due to bad weather conditions, and c) the time lost due to technical reasons for each month of the campaign. The middle and lower plots show the distributions of the monthly observed hours (exc. readout time and standard stars observations) and the LIF detections, respectively.

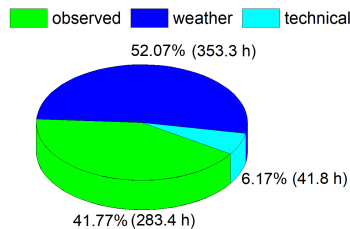


Fig. 2: Observations efficiency of the NELIOTA campaign between February 2017 and mid August 2023.

statistics for the period before August 2019 can be found in Paper III.

The total observing efficiency of NELIOTA is presented in a pie chart (Fig. 2) that shows the absolute values and the percentages of the observing time, the time lost due to bad weather conditions, and the time lost due to technical reasons since 2017. It should be noticed again, that the values concern the true time durations, meaning that readout time and time spent for standard stars are excluded. Moreover, we clarify that this pie chart concerns only the time windows of the nights (i.e., 20 min up to 5 h) dedicated to lunar observations and is not the global statistics of observations of the Kryoneri Observatory. In total, we have observed the Moon for 283.4 h (287 nights spent) which corresponds to 41.8% of the total true available time (678.5 h in 466 nights). The 52.1% of the total true available time was lost due to bad weather conditions and 6.2% due to technical issues.

3. Updated catalog and statistics of LIFs

The observational results for all the detected flashes between August 2019 - mid August 2023 are given in Table A.1. The LIFs are presented in chronological order (increasing number) and for each one we list: a) the date and the UT timing of the detection, b) the characterization for its validity (for details see Paper III), c) the maximum duration (t_{\max} in ms), d) the peak magnitudes in R and I passbands, and e) the selenographic coordinates, namely latitude ($Lat.$) and longitude ($Long.$). The light curves of the multiframe LIFs are illustrated in Fig. B.1.

It should be noted that in these tables there are a few cases of LIFs that, although detected in both passbands (#115, #119, #149, #178, #263), they are characterized as SC2. This is due to their very low $R - I$ index (less than 0.15), which leads to peak temperatures greater than 8500 K. As found in Paper III and will be shown later in Section 4, the typical evolved temperatures of LIFs are much lower than this value. An alternative explanation is that they are simply GEO satellites/debris crossing the FoV. Therefore, we consider these events as less likely suspected LIFs. Event #137 presented a very strange photometric behaviour. It was detected in five frames in both bands with a tiny magnitude variation from frame to frame and the $R - I$ indices varied between 0.28 and -0.26 . Moreover, a slight displacement between successive frames was detected but it was too small to be discarded directly as a moving object. We estimate that this event is more likely a GEO satellite/debris. Event #203 had a very elongated photometric profile and although it was relatively bright in the I passband (8.84 mag), it was detected only in one set of frames. Its $R - I$ index is 0.38 mag, which corresponds to a relatively high temperature of approximately 5800 K. Therefore, again, we cannot be certain for its nature and we simply prefer to consider it as a suspected LIF.

The magnitude distributions of the validated and the suspected LIFs for the given time-period are shown in Fig. 3. For reasons of completeness, this figure illustrates also the respective magnitude distributions since the start of NELIOTA operations in 2017. It should be noticed, that there are not any suspected flashes detected only in the R passband. Arguments for this can be found in Paper III/Section 3.1. As can be seen from the R passband distribution, the vast majority (73.4%) of the LIFs detected by NELIOTA range between 9-11 mag. The LIFs between 10-11 mag are 40.6% of the whole sample, while those between 11-12 mag are 8.3%. Therefore, our completeness limit is between 9-9.5 mag and 9.5-10 mag in the I passband for the validated and suspected LIFs, respectively, and between 10-10.5 mag in the R passband. It should be noted that the latter percentages show that approximately the half of the observed LIFs cannot be detected by small-size telescopes (i.e., with diameters of the order of a few tens of centimeters). These fainter LIFs are numerous and, as can be seen in the following section, their majority were produced by low-mass meteoroids, whose kinetic energies cannot be considered negligible in case of an impact with a space vehicle or a lunar base. As shown in the works of Brown et al. (2010) and Suggs et al. (2014), the lower the kinetic energies of the meteoroids, the higher their collision probability. The latter, assuming similar travel velocities of the sporadic meteoroids, can be also used for the mass population determination, that is the lower the masses of the meteoroids, the higher their populations. The latter is more or less what is expected from the evolution of the minor bodies. Obviously, the reason for not detecting more LIFs between 11-12 mag is the observation limit of our setup. The I passband distribution of the validated LIFs (Fig. 3-middle panel) shows clearly that the same LIFs in the

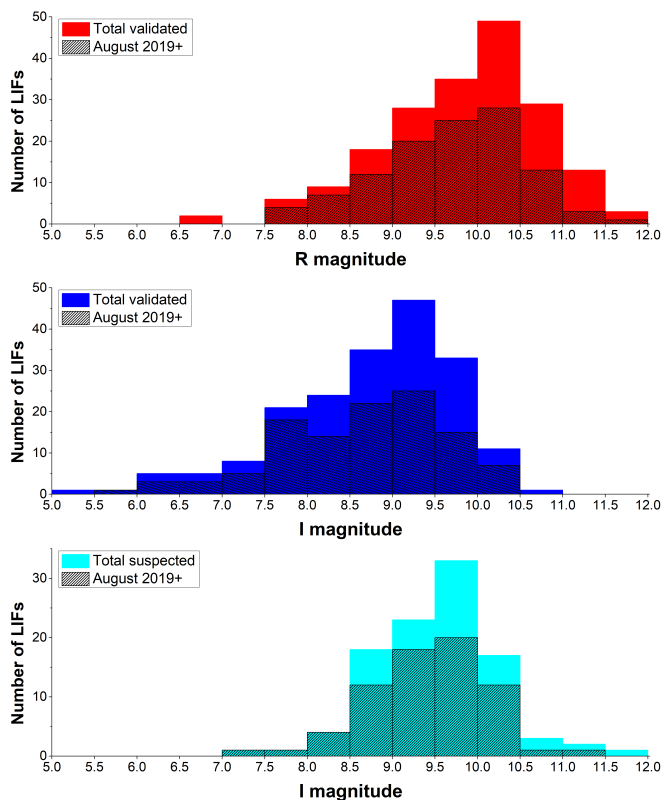


Fig. 3: Magnitude distributions of LIFs detected by NELIOTA since 2017 (colored patterns) and after July 2019 (black patterns). Upper and middle panels show the R and I passband magnitude distributions for the validated flashes. The lower panel is the I -mag distribution for the suspected flashes.

R passband are statistically one magnitude brighter in I . This confirms that the LIFs are relatively cool events, as concluded in Papers I and III. It should be noticed that in the I passband magnitude distribution of the validated LIFs (Fig. 3-middle panel), there is only a small number of detections between 10-11 mag. This is because, as mentioned before, the respective light emission in R passband is very close to our observational limit, hence they cannot be validated. On the other hand, the magnitude distribution of the suspected LIFs (Fig. 3-lower panel) shows that 19.6% range between 10-11 mag and 3.2% between 11-12 mag. The reason that we did not detect more suspected LIFs fainter than 10 mag is again our observational limit superimposed by the difficulty to distinguish faint suspected LIFs from low-energy cosmic rays or faint slow-moving satellites/debris.

The locations of the detected LIFs on Moon are shown in Fig. 4. This figure shows all detections of NELIOTA, while those that correspond to the time-period after July 2019 have an ID number greater than 113. LIFs with colors other than yellow denote that the impacting meteoroids were associated with active meteoroid streams during the time of the observations. For the latter, the method of Ortiz et al. (2015) and Madiedo et al. (2015a,b) was implemented (cf. Paper III). In this figure, LIFs that appear exactly on the limb or slightly out of it have longitude values greater than this background lunar map includes. Their locations were included in our FoV due to the lunar libration at the timing of the observations.

The detection limits of NELIOTA are not easy to be accurately determined. Although in Paper II we showed that using this equipment we can reach a magnitude of 12 in R passband,

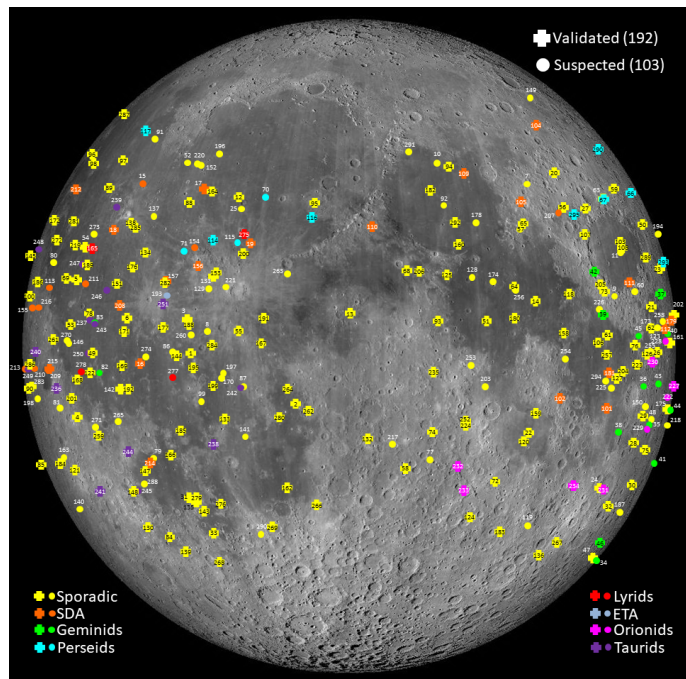


Fig. 4: Locations of LIFs detected by the NELIOTA campaign since February 2017. Detections after July 2019 have numbers greater than 113. Crosses and filled circles denote the validated and the suspected flashes, respectively. Different colors denote association of the projectiles with active meteoroid streams (see text for details and Paper III).

this limit varies because it depends on a) the lunar illumination phase, b) the local seeing conditions, c) the airmass of the Moon, d) the distance of the flash from the lunar terminator, that is, the dayside, and e) the Earth-Moon distance. Therefore, since the determination of our true detection limit is quite complex, we chose to present some graphs in order to obtain a qualitative view. The R magnitude detections of the validated LIFs as well as the estimated magnitudes of the suspected LIFs (see Section 4.1) against the lunar phase are illustrated in Fig. 5. Based on the validated LIFs, we clearly see that during the lunar phases in the ranges 110° - 150° and 210° - 250° that correspond to illumination phases 0.07-0.33, the upper limit of the detections is ~ 11.4 mag. However, there are three validated LIFs above this limit that probably concern extremely good observing conditions. Beyond these lunar phase values (i.e., $> 250^\circ$ and $< 110^\circ$), which correspond to illumination phases greater than 0.33, the detection limit drops approximately 1 mag. Similarly to the previous range, there are also two validated LIFs above this threshold. Regarding the suspected (estimated R magnitudes) LIFs, their majority lie well above our detection limits regardless the lunar phase. However, there are many expected detections below our limits. For these suspected flashes we argue that the aforementioned parameters (b, c, and d) prevented their detection or their R magnitudes were actually fainter than estimated.

The turning points of the accumulation distributions of LIFs in Fig. 6 can be used to roughly determine the detection limit of NELIOTA. For the R passband, the turning point is at $m_R \sim 11.2$ mag, and after that there is a slight increasing part that reaches up to ~ 12 mag. Therefore, we can estimate that, indeed, NELIOTA can marginally detect LIFs up to that magnitude, but, in general, can easily detect LIFs up to 11.2 mag in R passband. Regarding the limiting I magnitude, we use the LIFs of the sus-

pected and validated LIFs because, as mentioned before, the suspected LIFs were probably too cool to be detected in R passband as well. Hence, their inclusion provides more complete information regarding the limiting I magnitude. The grey data points distribution in Fig. 6 has a turning point at ~ 10.2 mag and, similarly to R passband, this is followed by a slight increasing part that ends to ~ 11.6 mag. Therefore, we can plausibly conclude that our setup can typically detect LIFs up to $m_I \sim 10.2$ mag, and in very good observing conditions (e.g., low illumination phase, low airmass) can reach up to ~ 11.6 mag.

The distribution of the detected LIFs in the I filter against the lunar and illumination phases is illustrated in Fig. 7. The highest signal-to-noise ratio for a given magnitude of a LIF will be obtained close to new Moon, that is for illumination phases less than 0.18 (3-4 days past or before new Moon). Even though the background brightness due to Earthshine is the highest close to new Moon, the straylight from the illuminated part will be the lowest, hence the contrast of a LIF can be very high, even for a faint one. However, the duration of the observations during these phase parts is very short, typically less than 1 h. It should be noted that the Earthshine produces approximately 7-10 orders of magnitude less luminous energy flux than a typical LIF with a peak temperature between 2000-5000 K (Bouley et al. 2012), so it can be considered negligible. On the other hand, for illumination phases greater than 0.33 (5-7 days past or before new Moon) the observation duration is the longest possible (order of a few hours). However, the straylight of the dayside of the Moon increases the lunar background that much, so the LIFs are very hard to detect (see also Fig. 5). In addition, when the Moon is close to the apogee (i.e., increased photons flux per pixel), the telescope has to point further away from the lunar terminator in order to avoid extremely high background values. Because of the latter, less lunar surface is covered. Therefore, according to Figs. 5 and 7, the best balance between the observations duration and lunar phases is achieved between approximately 0.20-0.35 illumination phases.

The distribution of the magnitudes of the suspected and validated LIFs in the I passband against the lunar illumination phase and their longitude is plotted in Fig. 8. This plot was made in order to examine any dependence of the LIF detections on their distance to the lunar terminator. It should be noticed that this distribution is biased due to the fact that our setup covers only a portion of the full Moon disk. The majority of the detections were made between $\pm 20^\circ$ and $\pm 80^\circ$ longitude values. This can be explained by the lunar area coverage of our setup and the distance of the detections from the lunar terminator. Longitudes between -20° and 20° are always closer to the lunar terminator, thus, the lunar background is always higher, hence the detection is more difficult. Moreover, regions close to the lunar center are included only when the Moon is close to the apogee, implying that more lunar surface is included in the FoV. On the other hand, when Moon is close to the apogee, more light is gathered in the pixels, hence, again, increased lunar background values are met. Detections in longitudes greater than $+80^\circ$ and less than -80° depend on the lunar libration at the time of the observations. We also see that LIFs brighter than 9 mag can be detected under all circumstances. More or less the same stands for LIFs between 9-10 mag with a slight difference that they seem to be favored by illumination phases between 0.2-0.35 (due to longer observations duration) and are mostly located in regions with longitudes greater than 20° and less than -20° . The majority of the LIFs fainter than 10 mag can be detected mostly during lunar illumination phases lower than 0.35 and at longitudes greater than 30° .

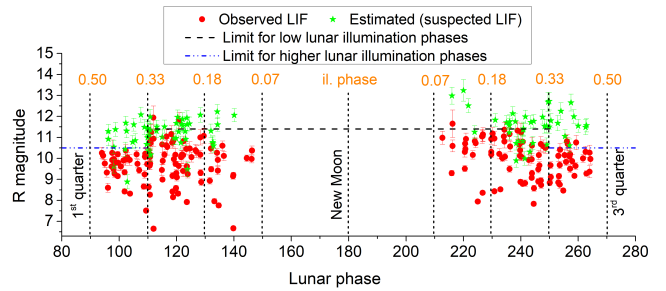


Fig. 5: R passband magnitudes of validated (red points) and suspected (green stars) LIFs, observed since February 2017, against the lunar phase. Horizontal dashed lines indicate the empirically set detection limits of NELIOTA in R filter according to the lunar phase (see text for details). Vertical short-dashed lines denote the range of the lunar phases during which NELIOTA was operating. For convenience, the respective illumination phases are also indicated (orange).

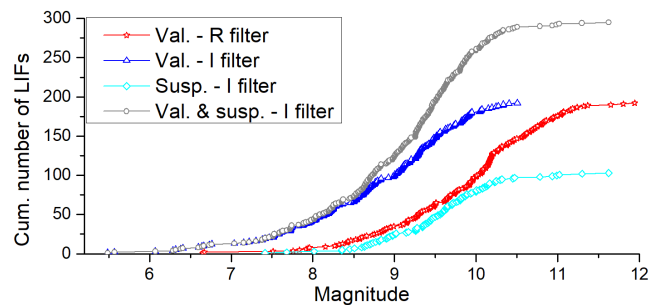


Fig. 6: Cumulative number of LIFs detected by the whole NELIOTA campaign (283.4 h of lunar monitoring) according to their peak magnitude values. Different colors denote different observed passbands and validation characterizations.

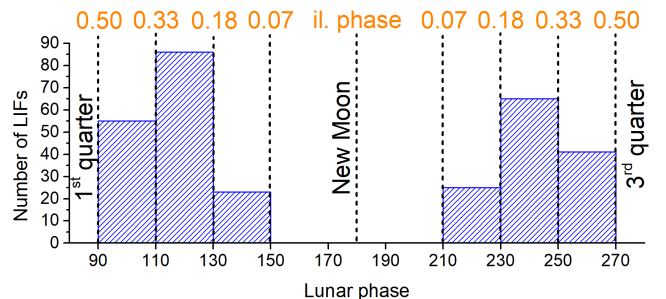


Fig. 7: Distribution of validated and suspected LIFs (I passband), observed since February 2017, as a function the lunar and illumination phases.

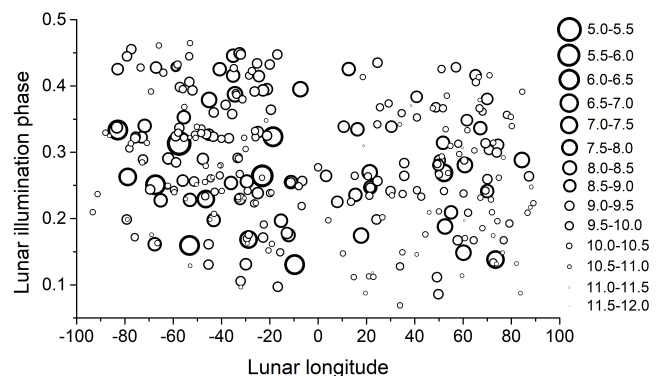


Fig. 8: Distribution of validated and suspected LIFs (I passband) against lunar longitude and illumination phase. The bigger the symbol the brighter the LIF.

It should be noticed that there are slightly more LIFs detections in the western hemisphere of the Moon (see Figs. 4 and 8). Particularly, 163 out of 295 LIFs (validated and suspected) were observed in this hemisphere, which results in a percentage of 55.3%. This is explained by the slightly longer observing time spent in this hemisphere, totally by chance, that is 145.97 h out of 283.4 h (51.5%). Therefore, we justify that the detections of LIFs are independent of the observed hemisphere, hence, it can be concluded that the Moon is bombarded homogeneously.

4. Physical parameters

4.1. Calculation methods

We proceed to compute the physical properties of the impacting projectiles (i.e., masses, radii) that produced the observed LIFs after July 2019, the temperatures evolved during their impacts, and the sizes of the expected craters. The total luminous energies of the LIFs were calculated as described in Paper III (Section 6.2), then their temperatures according to the photon fluxes from the *R* and *I* passbands (i.e., their magnitudes; see Papers I and III).

The peak magnitudes and peak temperatures of the detected LIFs are given in Tables A.1-A.3. It should be noticed that these temperature values are not always derived by the respective peak magnitudes given in the same table. There are indeed cases (LIF #191, #209) whose peak magnitudes resulted in a cooler temperature value than that derived from other sets of *R* and *I* frames. The magnitudes and the temperatures of the multiframe flashes are given in Table B.1, their light curves in Fig. B.1, and their temperature curves in Fig. B.2.

For the calculation of the kinetic energy (KE_p) of the meteoroids we assumed various values for the luminous efficiency η within the range $5 \times 10^{-4} < \eta < 5 \times 10^{-3}$ (Bellot Rubio et al. 2000a,b; Ortiz et al. 2006; Moser et al. 2011; Swift et al. 2011; Bouley et al. 2012; Suggs et al. 2014; Madiedo et al. 2015b, 2017, 2018, 2019). Subsequently, for the cases associated with meteoroid streams, the mass values were derived from the KE_p assuming velocities (V_p) according to the streams of origin. For sporadic meteoroids, an impact velocity of 17 km s^{-1} was assumed (Suggs et al. 2014). For the radii calculation we, again, assumed densities (ρ_p) according to the parent bodies of the stream meteoroids and a value of 1.8 g cm^{-3} for the sporadics. These assumed values were taken by Babadzhanyan & Kokhirova (2009) and for convenience of the reader are also listed in the appendix (Table C.1). The expected crater sizes were calculated using the scaling law of Gault (1974) (cf. Melosh 1989) with the assumption of an impacting angle of 45° .

The results for the validated flashes are given in Table A.2, which are divided into two main parts and organized as follows: The first part (first five columns) contains the ID number of the LIF, its possible association with a meteoroid stream (see Section 2 and Paper III for details), the calculated luminous energy per observed passband (LE_R and LE_I) and the peak temperature of the impact. The second part of this table lists the physical parameters of the impacting meteoroids, which are their kinetic energy (KE_p), mass (m_p), radius (r_p), and the expected crater size (d_c) for three different values of the luminous efficiency η . The complete formalism for the aforementioned methods is given in Paper III/Sections 6.2.1 and 6.4. The respective results for the first 79 validated LIFs can be also found in that work.

For a rough estimation of the physical parameters of the suspected flashes we based on the updated luminous energies per band correlation of the validated LIFs using the whole sample of

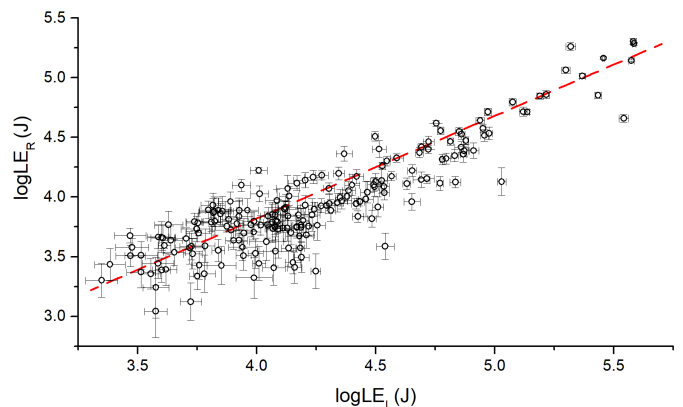


Fig. 9: Correlation between emitted energies in *R* and *I* passbands of the validated LIFs detected by NELIOTA since 2017.

LIFs detected by NELIOTA (cf. Paper III). The data points are plotted in Fig. 9 and using linear fitting we derive the following relation:

$$\log LE_R = 0.38(9) + 0.86(2) \log LE_I \text{ with } r = 0.96, \quad (1)$$

where r is the (Pearson's) correlation coefficient. Comparing Eq. 1 with that from Paper III, we notice that using larger sample, the two relations are in agreement but we constrained more (i.e., smaller error values) both the intercept and the slope, while r is increased by $\sim 6.7\%$. Using the above relation and the observed LE_I of the suspected LIFs, we are able to estimate the emitted $LE_{R, \text{est}}$. Subsequently, we calculate the photon flux in the *R* passband and convert it to apparent magnitude $m_{R, \text{est}}$ (for method see Paper III/Secs 6.1 and 6.2.2). Therefore, based on the same assumptions for η , V_p , and ρ_p , as in the cases of the validated LIFs, we are able to roughly estimate the temperature (T_{est}) developed during the impact, the kinetic energy ($KE_{p, \text{est}}$), the mass ($m_{p, \text{est}}$), and the radius ($r_{p, \text{est}}$) of the impacting meteoroids. Finally, we also estimate the size of the expected formed craters ($d_{c, \text{est}}$). The aforementioned values are listed in Table A.3 for $\eta = 1.5 \times 10^{-3}$. Despite the fact that the parameters of the first 33 suspected LIFs (Table A.3) had been also presented in Paper III, they are re-calculated and presented herein for reasons of consistency due to the update of the luminous energies relation (eq. 1). The SC2 LIFs #52, #70, #71, #81, #115, #119, #137, #149, #178, #203, #263 were excluded from this table since their nature is rather ambiguous (see Paper III for the first four ones and Section 2 for the rest).

4.2. Statistics of the physical properties of the meteoroids and impacts

The distribution of the peak temperatures of the validated LIFs and the respective (estimated) one of the suspected LIFs are shown in Fig. 10. A significant portion (45.8%) of the validated LIFs evolved peak temperatures between 2500-3500 K. It should be noticed that 84.9% of the whole sample of the validated LIFs range between 2000-4500 K. Only 3.6% of this sample resulted in temperatures lower than 2000 K, and only 11.5% higher than 4500 K. The drop off of low temperature values is due to our observing setup. Low temperature values result, in general, from LIFs with faint *R* magnitudes, that is $R - I > 1.91 \text{ mag}$. So, given that the majority of the suspected flashes range between 9-10 mag in the *I* passband (see Fig. 3), it is very possible that

the LIFs were not detected in the R passband due to observations limitations (see also Fig. 5). The estimated peak temperatures of the suspected LIFs (see Section 4.1 for details) in the same figure show a distribution with a peak between 1500-2000 K. It should be noted that these temperatures can be considered as upper limits, since we estimated the expected magnitudes of these flashes in the R passband using eq. 1 (see Sect. 4.1 for details). The LE_1 of the suspected flashes (i.e., those that were not detected in the R passband) are within the range shown in Fig. 9. The true LE_R and R magnitude values should be lower and fainter than the estimated ones, respectively, implying higher $R - I$ indices, hence lower temperatures for the suspected LIFs. We note that the peak of the flash (i.e., brightest magnitude and highest temperature phase) might have occurred during the readout of the camera and might have been missed in the observations. Nevertheless, the current values of the peak temperatures of the validated LIFs can be considered as lower limits and a detailed discussion for this is made in Section 7.

The meteoroid mass distribution for $\eta = 1.5 \times 10^{-3}$ and for various mass ranges is illustrated in Fig. 11. The choice of this η value is based on the fact that it stands almost between the two extreme values ($5 \times 10^{-4} < \eta < 5 \times 10^{-3}$) and is widely used as reference. However, in Table A.2, the masses, radii, and crater sizes have also been calculated for both these extreme η values. For convenience, we notify the reader that the extreme η values rescale the masses (Fig. 11) by a factor or a fraction of ~ 3 . This figure shows that the derived meteoroid masses range from ~ 2 g up to ~ 2.7 kg, but it can be clearly seen that the vast majority weighs less than 200 g. The distribution for the latter range is plotted in the internal panel of the same figure. A fraction of 60.4% of the meteoroids that produced validated LIFs weigh up to 100 g and they are distributed almost homogeneously into bins of 25 g. The 76.6% of the whole sample have masses less than 200 g, and the 88% less than 400 g. Moreover, as expected from their magnitudes (mass-magnitude correlation, cf. Paper III and Section 5), the masses of the meteoroids of the suspected LIFs have systematically lower values, typically less than 50 g.

Similarly to the mass distribution plots, the radius distributions of the meteoroids produced the observed LIFs are plotted in Fig. 12 for $\eta = 1.5 \times 10^{-3}$. Note that the plotted radius values in this figure have a multiplication factor of ~ 1.49 with respect to those that can be derived using $\eta = 5 \times 10^{-3}$ and a division factor of ~ 1.44 for those with $\eta = 5 \times 10^{-4}$. This figure shows that the radii of the projectiles range between 0.7-6.95 cm. The vast majority (69.8%) of the validated meteoroids and almost all of the suspected have radii less than 3 cm. Therefore, and in order to have an analogy with the real life item sizes, the majority of the validated meteoroids have sizes roughly between a sphere with a diameter similar to the coin of 2€ (2.575 cm) and a tennis ball (6.54 cm). Only 1.5% have sizes less than 2.8 cm in diameter (i.e., spheres with sizes similar to the smaller coins of 1€). The 11.9% of the whole sample have sizes between tennis and baseball balls (diameters 6-8 cm), and only 4.1% may reach the size of a shotput ball (13 cm).

The distribution of the expected crater sizes due to the observed meteoroid impacts (for an impacting angle of 45°) is illustrated in Fig. 13. For the validated LIFs, the size range is estimated to be between 1-6 m. However, there is a clear peak between 1.5-2 m for both validated and suspected LIFs.

Based on our relatively large sample of multiframe LIFs, we attempted to make a comparison of their light curve profiles in order to check whether any systematic behaviour occurs. We included only the LIFs for which at least four frames in the I -passband were recorded and they are illustrated in Fig. 14. The

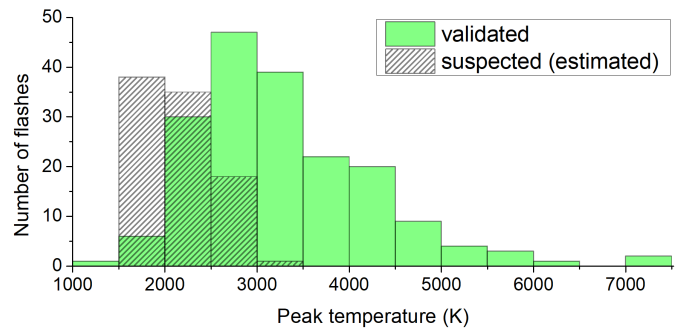


Fig. 10: Peak temperature distributions of validated and suspected LIFs detected by NELIOTA since 2017.

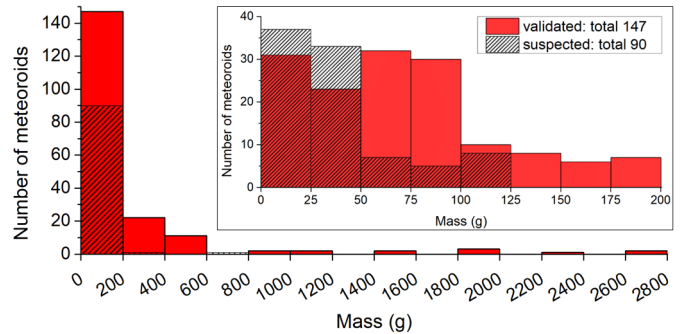


Fig. 11: Mass distributions of meteoroids producing the observed LIFs for different ranges (samples) and for $\eta = 1.5 \times 10^{-3}$.

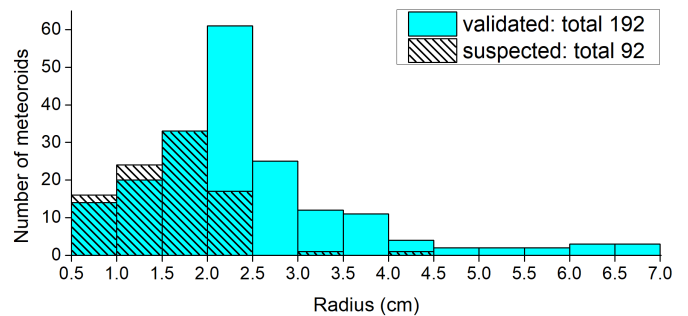


Fig. 12: Radius distribution of meteoroids producing the observed LIFs for $\eta = 1.5 \times 10^{-3}$.

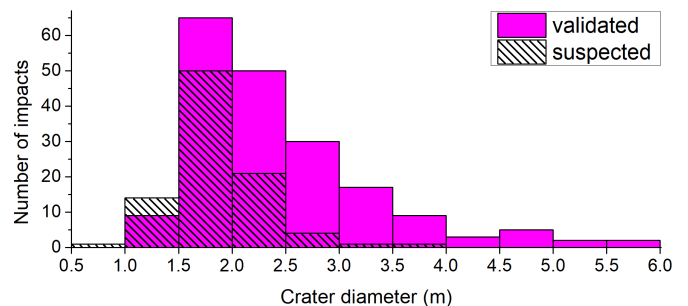


Fig. 13: Distribution of expected crater sizes of the observed LIFs.

selection of the sample is based on the frame multiplicity of the LIFs in order to minimize the error of not recording all the emitted light of the first and last frames due to the readout time of the camera. The individual light curves (with the error bars) for LIFs with ID number less than 114 are given in Paper III, while the

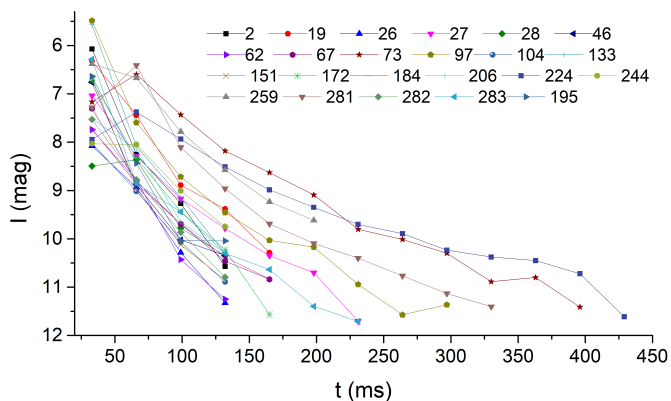


Fig. 14: Light curves of multiframe LIFs lasting more than four frames in the I -passband.

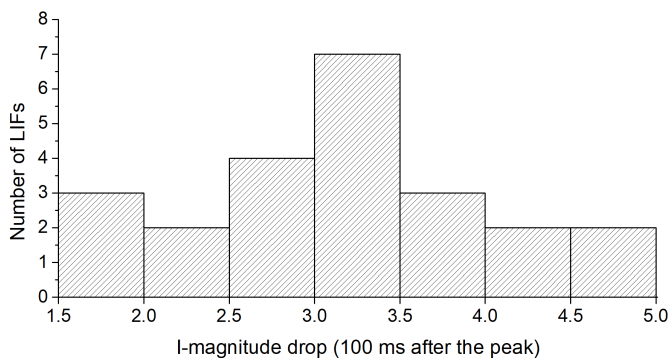


Fig. 15: Histogram of magnitude drop in the I -passband 100 ms after the peak magnitude. The sample consists of the LIFs shown in Fig. 14.

rest are plotted in Fig. B.1. These profiles all present a similar exponential decrease, which we attempt to quantify by measuring the brightness decrease 100 ms after the observed peak brightness. The histogram of the decline rate distribution (Fig. 15) appears to be a normal distribution with a peak value around ~ 3 mag. Additional correlations between their masses and temperatures and their decline rates were attempted but the results were negative.

Regarding the temperature evolution of the LIFs, we notice that most of the LIFs presented in this work show a temperature decrease (Fig. B.2), but the cooling rate is not the same. Moreover, there are six cases (LIF #172, #191, #209, #224, #283, #287), whose temperature increased between the first and the second set of frames indicating that the recording of the impact began before the occurrence of the maximum temperature. Finally, there are also a few cases (LIF #224, #259, #281), in which after an initial decrease of the temperature, a constant temperature time period occurred. In addition, a temperature increase was observed before they completely vanish in the R passband. Similar to the previous plot, we tried to find any trends in the temperature evolution behaviour of the LIFs. For this, only the multiframe LIFs in both passbands were used (i.e., 30 LIFs in total). In order to avoid a dense diagram, we plotted in Fig. 16 only those that lasted more than two frames in both passbands. Individual temperature evolution curves for LIFs with ID number greater than 113 are illustrated in Fig. B.2 and the rest are shown in Paper III. The histogram of all the aforementioned multiframe LIFs regarding their temperature variation between the peak temperature and the next 33 ms is given in Fig. 17. This

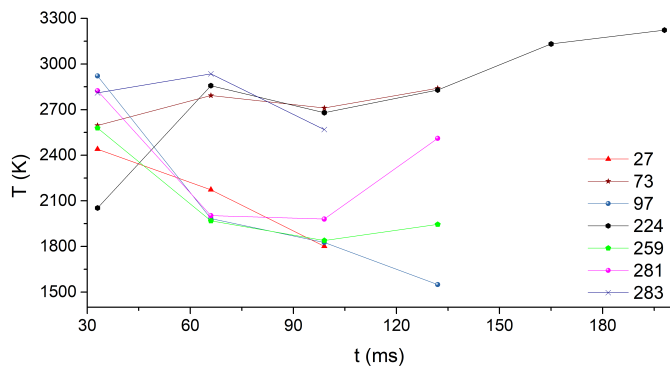


Fig. 16: Temperature curves of multiframe LIFs lasting at least three frames in both passbands.

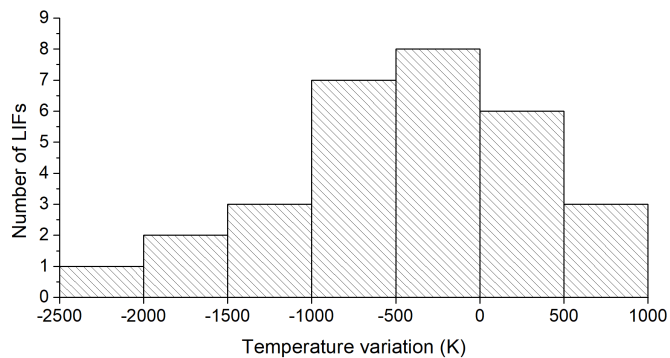


Fig. 17: Histogram of temperature variation of 30 multiframe LIFs in both passbands. The variation concerns the first 33 ms after the peak temperature.

plot shows that the majority of these LIFs have relatively slow cooling rates (i.e., between 0 and -1000 K). On the contrary, there are many that after their peak temperature not only did not show any cooling trend, but, on the contrary, they presented a slight increase. However, it should be noted that the temperature errors are quite large and that our sample is relatively small to provide concrete conclusions. For the cases of LIFs with constant or increasing temperature, we assume that this thermal behaviour is somehow connected to the material, for example the cooler plume initially covering the hotter plume.

5. Correlations between physical parameters

The mass-magnitude correlation of LIFs is quite useful since it provides a direct sense of the meteoroid mass that produced the observed LIF. However, the mass calculation is not straightforward since the lost energy during the readout time of the camera and the LE of all the observed passbands should be taken into account (cf. Paper III). Using our sample, we are able to derive empirical relations between masses (m_p) of the projectiles and peak magnitudes of the LIFs (m_R , m_I). These relations can be used from other observers to estimate the masses of the meteoroids producing LIFs as long as they use the R or I filters. The meteoroid masses against their respective peak magnitudes in the observed passbands are plotted in Fig. 18. The data points in this figure form parallel layers based on their velocities. Therefore, in order to calculate the correlation between the aforementioned quantities, we used only the data of the sporadic LIFs (black points in Fig. 18). Using $\eta = 1.5 \times 10^{-3}$ and various values for the impact velocities, different masses are derived for the spo-

Table 1: Intercept values of Eqs. 2-3 according to the impact velocity of the meteoroids based on their origin.

Origin	V_p (km s^{-1})	A_R (mag)	A_I (mag)
SPO	17	6.6(2)	5.9(1)
SPO	24	6.3(2)	5.6(1)
Tau	28	6.1(2)	5.5(1)
Gem-SDA	38	5.9(2)	5.2(1)
Lyr	49	5.6(2)	5.0(1)
Per	61	5.5(2)	4.8(1)
Ori	67	5.4(2)	4.7(1)

radic meteoroids, hence, different linear fittings were made. The fitting curves are plotted in the same figure and correspond to $V_p = 17$ and 24 km s^{-1} (i.e., extreme values of the sporadic meteoroids) as well as to the velocities of the stream meteoroids (see Table C.1). The slope values of the linear fittings for the data of each passband were the same regardless the assumed velocity. On the contrary, the intercept value (A) was changing. Therefore, we derive the following relations:

$$\log m_p = A_R - 0.45(2)m_R, \text{ with } r = 0.91, \quad (2)$$

for the R passband and

$$\log m_p = A_I - 0.44(1)m_I, \text{ with } r = 0.95, \quad (3)$$

for the I passband. The intercept values (A) for each assumed velocity and for each passband are listed in Table 1.

Similarly to Paper III, we attempt to find a possible correlation between the physical parameters of the meteoroids and the peak temperatures of the LIFs using the whole sample of the validated flashes. First, we begin with a correlation between the observed peak magnitudes and the peak temperatures of the observed LIFs. This attempt is illustrated in Fig. 19 that shows the 3D correlation of the peak R and I magnitudes with the temperature. It should be noticed that the horizontal plane (i.e., I - R mag–blue points) of this figure corresponds more or less to the plot of Fig. 9, since the LE of each band is connected to the respective peak magnitude (cf. Paper III). The projection of the sample on the R mag vs T plane (red points) is also shown. We notice that for brighter R magnitudes (i.e., < 8 mag) the LIFs tend to have lower temperatures. For fainter LIFs, we notice that there is a slightly increasing trend of the temperature. However, we argue that this trend is apparent and biased from our detection limits. Low-temperature LIFs (i.e., $T < 3000$ K) are easier to be detected when they are bright, since their emission in R passband will be always under our detection limit. On the contrary, similar temperature LIFs but fainter than approximately 10 mag in the R filter, although they can be potentially detected in I passband, they cannot be validated. We may also notice that the aforementioned trend begins after $R \sim 8$ mag. This is due to the fact that higher temperatures LIFs emit more in R filter, thus, are easier to detect.

One of the conclusions of Paper III concerned the noncorrelation between the masses of the meteoroids and the impact temperatures regardless the impact site. Again, using an almost triple sample of validated LIFs, we update this diagram, but, again, no obvious correlation has been found (Fig. D.1). Moreover, we searched for a correlation between the meteoroid sizes and peak temperatures, since their contact surface may play a role. In agreement with the mass-temperature plot, this correlation shows that the peak temperature is more or less independent

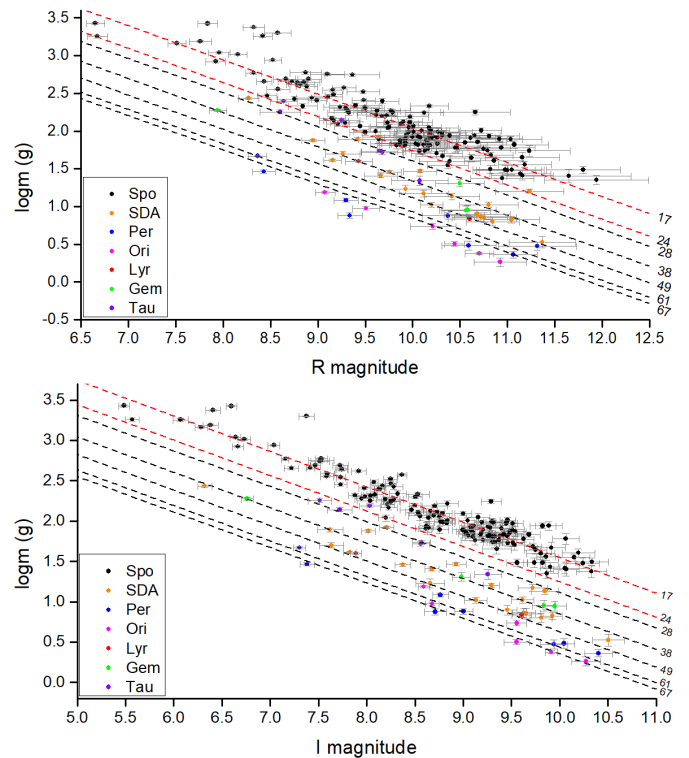


Fig. 18: Correlations between peak magnitudes in R (upper panel) and I (lower panel) passbands and meteoroid masses for $\eta = 1.5 \times 10^{-3}$. For the plotting of the sporadic meteoroids an impact velocity of 17 km s^{-1} was assumed. The masses of the stream meteoroids are based on the velocities given in Table 1. The assumed velocities are indicated next to each fitting curve.

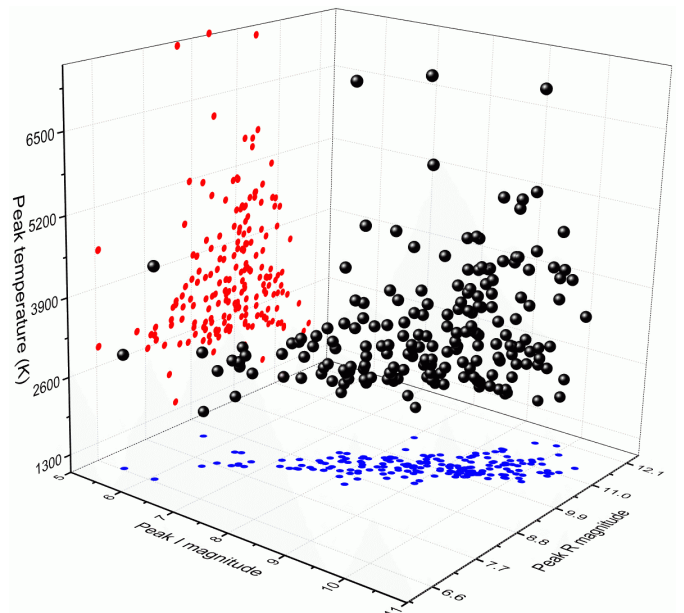


Fig. 19: Three-dimensional correlation of peak magnitudes in R and I passbands with the peak temperatures of the LIFs.

of the impact site no matter the size of the projectile (Fig. D.2). However, we notice a peak slightly before $T = 3000$ K and a steep decrease of the sizes with the increasing temperature, something that is not that clear in the previous plot. For the aforementioned plots, we assigned colors to the data points according

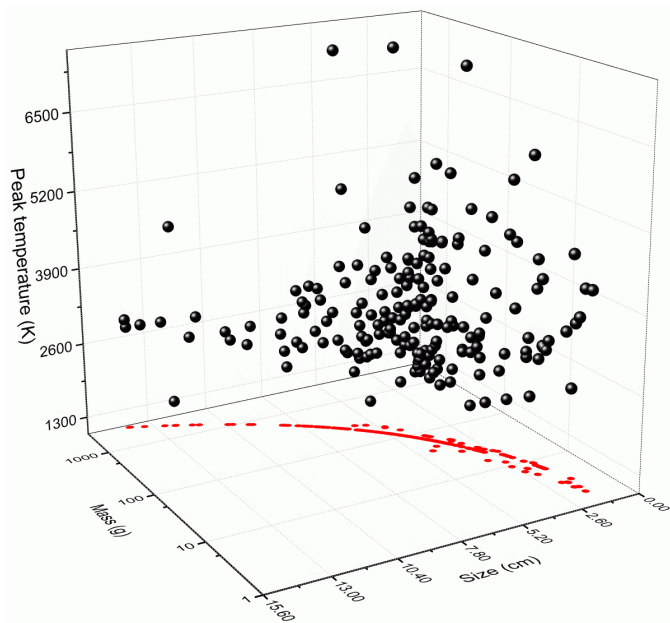


Fig. 20: Three-dimensional correlation of mass and size of the meteoroids with the peak temperature evolved during the impacts.

to visual inspection of the impact area. Dark areas on Moon corresponds mostly to the maria regions, while grey or bright to more rocky/mountainous regions. However, the 3D plot illustrated in Fig. 20 combines the above two diagrams and shows that the evolved temperature is independent of or even anticorrelated to the mass and size of the projectiles. A short discussion on this result is given in Section 7.

6. Meteoroid appearance frequency, impact probability and hazard estimation

In this section we focus on the LIF detection rates of NELIOTA that lead to the calculation of the meteoroid appearance frequency on the Moon and around Earth. In Table 2 we list the total observed hours on the Moon and the number of the respective LIF detections during normal periods of time (*Spo*) and during the passages of the Earth-Moon system through meteoroid streams (*Str*). Moreover, for each case we list both the number of validated LIFs and the number of the validated and suspected LIFs. The latter values can be considered as the upper limits. In order to be more direct, the respective detection rates (*Det. Rate*) for each case have been calculated and listed in the same table. These rates strongly depend on our FoV, hence the covered lunar area by our setup (see Section 2), and are given only for a direct sense of what we can achieve with such equipment. In order for these rates to be comparable with others of similar campaigns (Suggs et al. 2014; Rembold & Ryan 2015), they are normalized to the covered lunar surface (i.e., per squared kilometer). As mentioned in Paper III, the covered lunar area is not constant, since it depends on the Moon-Earth distance (i.e., variation of the pixel scale) and the lunar illumination phase (i.e., phases greater than 0.35 require repositioning of the telescope in order to avoid brighter areas). Therefore, the normalised detection rates (*Norm. Rate*) in Table 2 have been calculated using an approximate lunar covered area of 3.11×10^6 km² by our setup that corresponds to an Earth-Moon distance of 3.84×10^5 km. The

Table 2: Flash detection rates of NELIOTA according to the origin of the meteoroids.

	Validated			Validated and suspected		
	Spo	Str	Sum	Spo	Str	Sum
Obs. Hours	237.8	45.6	283.4	237.8	45.6	283.4
Detections	145	47	192	208	87	295
Det. Rate ^a	0.6	1.0	0.7	0.9	1.9	1.0
Norm. Rate ^b	1.96	3.32	2.18	2.81	6.14	3.35

Notes. ^aIn units of LIF h⁻¹, ^bin units of 10⁻⁷ LIF h⁻¹ km⁻², Spo = sporadic, Str = stream.

Table 3: Appearance frequencies of meteoroids on the Moon and around Earth in units of meteoroid h⁻¹.

		Earth				
		Moon	MS	LEO	MEO	GEO
Altitude (km)	Sur	0	80	500	20000	36000
Validated	Spo	7.4	102	116	1712	4420
	Str	12.6	173	197	2898	7481
Validated and suspected	Spo	10.7	147	167	2456	6341
	Str	23.3	321	364	5364	13848

Notes. Spo = sporadic, Str = stream, Sur = surface, MS = Mesosphere, LEO/MEO/GEO = Low/Medium/Geosynchronous Earth Orbit.

slight discrepancy between the current detection rates and those from Paper III (Table 2) are clearly due to the current larger sample used.

As concluded in Section 2, we can plausibly assume that the Moon, hence Earth, is bombarded homogeneously by meteoroids. Using this assumption and the sporadic and the stream normalised LIF detection rates of Table 2, we calculate and list in Table 3 the meteoroid appearance frequencies on the lunar surface and in the vicinity of the Earth. In this table, we present the calculations for both the validated and the validated and the suspected LIFs. Regarding the frequency appearance close to Earth, the calculations concern some typical distances from Earth's surface, such as the upper zone of the mesosphere (80 km), where meteors occur, the Low-Earth Orbit zone (LEO) at an altitude of 500 km, the Medium-Earth Orbit zone (MEO) at an altitude of 20000 km, and the Geosynchronous/Geostationary Earth-Orbit zone at 36000 km. The aforementioned meteoroid appearance frequencies are plotted in Fig. 21, which show how many meteoroids per hour enter a sphere with radius that has the size of the sum of the radius of the Earth and the distance from its surface (altitude).

Based on these appearance frequency rates, we attempt to calculate the probability of a meteoroid impact with a hypothetical infrastructure on the Moon or an orbiting satellite for various dimensions of the impacting target (effective surface) and the duration of the mission. Obviously, the meteoroid size (effective surface) is negligible in comparison with that of the impacting area, hence, it is not taken into account. Therefore, the impact probability can be calculated using the following formula:

$$P_{\text{impact}} = \frac{S_{\text{impact}}}{S_{\text{total}}} f_{\text{app}} t, \quad (4)$$

where S_{impact} is the effective impacting surface, S_{total} the total surface of the sphere (e.g., Moon) with a radius equal to that used to derive the respective calculated appearance frequency of the meteoroids f_{app} (Table 3), and t the time of the mission.

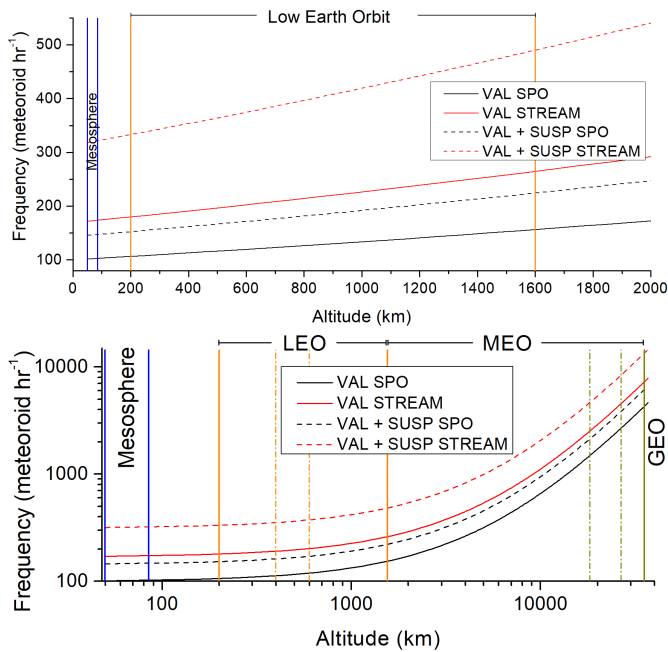


Fig. 21: Appearance frequency distributions of meteoroids around Earth up to an altitude of 2000 km (upper panel) and up to 36000 km (lower panel). Black and red lines denote the sporadic and the stream meteoroids, respectively. Solid lines correspond to the frequencies based on only the validated flashes, while dashed lines those that are based on the validated and suspected flashes. Vertical solid lines indicate the boundaries of the mesosphere, LEO, MEO, and GEO zones. Vertical dashed lines in the lower panel indicate satellite crowded orbit zones.

Regarding the impact on lunar potential infrastructures (e.g., buildings), we calculated the probabilities for different surface areas ranging from a small building (30 m^2) up to a large-size building with dimensions of a (european) football field (8000 m^2). For a meteoroid collision with a satellite, we took into account the size of the satellites with fully deployed solar panels, therefore, the calculations were made for the following effective surface areas: 30 m^2 (e.g., Starlink satellite), 500 m^2 , 2500 m^2 , and 8000 m^2 (e.g., International Space Station). Obviously, the calculated probabilities depend only on the effective surface areas and the respective appearance frequency and not on the distance (orbit). The collision probabilities against time are drawn in Fig. 22 for sporadic and stream meteoroids based on the detection of the validated and the validated and suspected LIFs.

The kinetic energies against the masses of the meteoroids producing the observed LIFs are illustrated in Fig. 23. Although these quantities are correlated via a power law, it is useful to plot them in order to get a rough idea of the range of the meteoroid carrying energies, hence, the potential damage on a satellite or on a lunar base that can be caused by a meteoroid impact. The velocities are based on the same aforementioned assumptions regarding the origin of the meteoroids, while the data points are calculated for various η values. Similarly to Fig. 18, we notice layers of data points corresponding to different origins of meteoroids (i.e., to different velocities). We notice that the KE of the projectiles can range between 0.8 MJ and 1.05 GJ . In this plot, we also indicate some representative energies of manmade explosions. Therefore, we notice that the majority of the mete-

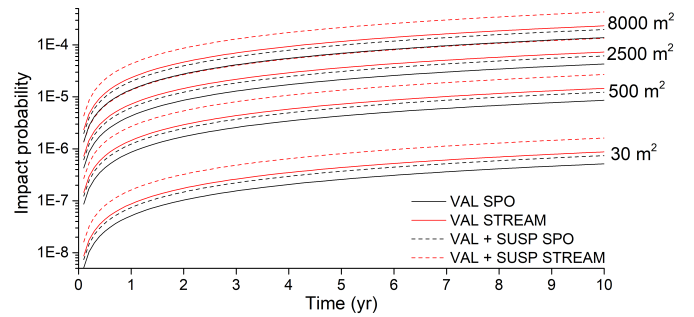


Fig. 22: Impact probability of a meteoroid with a potential infrastructure on the lunar surface or with a satellite in orbit around Earth for various impact surface areas (30 m^2 –small size building or satellite, 500 m^2 , 2500 m^2 –medium size building or satellite, 10000 m^2 –large size building or ISS size satellite). Colors and line styles denote the same as in Fig. 21.

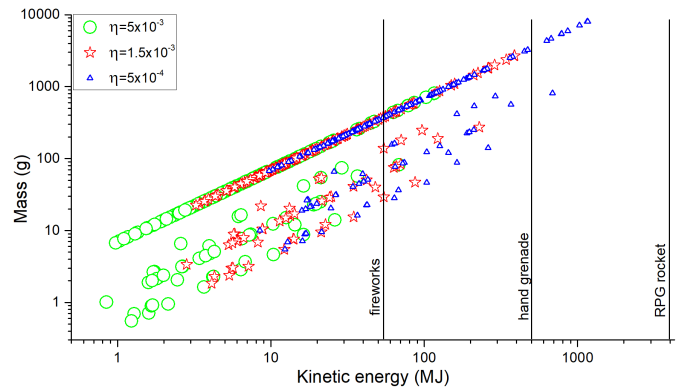


Fig. 23: Kinetic energies against masses for the meteoroids producing LIFs observed by NELIOTA for various η values. Representative energies are also indicated for estimating the damage that a meteoroid impact may cause. We note that the muzzle energies of typical weapons (e.g., pistols, rifles) or stronger military weapons (e.g., machine guns) are less than $3\text{--}5 \text{ KJ}$, i.e., two order of magnitudes lower than the minimum energy that the plot covers.

oids may cause serious damage to both satellites and potential infrastructure on the Moon.

7. Discussion

NELIOTA was monitoring the Moon for LIFs continuously for 6.5 yr using the largest telescope in the world (1.2 m Kryoneri telescope) dedicated to this kind of studies. This project was the longer systematic campaign for LIFs worldwide and produced an extremely large amount of data (more than 215 TB of lunar images) that were publicly available within 24 h after each observing night. Due to the large mirror size, it extended our knowledge for LIFs up to two magnitudes in R band, in comparison with other campaigns, while due to the dualband observations produced coherent statistics about the evolved temperatures during the impacts. The NASA Meteoroid Environment Office mentions 443 candidate impact flash events between 2005–2020 in their official webpage⁷, but no details are given. Therefore, the detection efficiency of NELIOTA can be

⁷ https://www.nasa.gov/centers/marshall/news/lunar/lunar_impacts.html

compared only with teams that presented their results in a published paper, such as Suggs et al. (2014) from NASA Meteoroid Environment Office and Rembold & Ryan (2015). The former team published a detection rate of 1.03×10^{-7} meteoroids $\text{h}^{-1} \text{km}^{-2}$ and the latter 1.09×10^{-7} meteoroids $\text{h}^{-1} \text{km}^{-2}$. It should be reminded that both teams used smaller size telescopes (30-50 cm). Sadly, these teams did not present any rates according to the meteoroid stream activity, so their rates are the simple division of the number of detections over the observed hours and covered lunar area. In order to be directly comparable with these teams, we presented in Table 2 the respective rates (Sum). We claim that in the conservative scenario that is based only on the validated flashes, NELIOTA has a detection rate of 2.18×10^{-7} meteoroids $\text{h}^{-1} \text{km}^{-2}$, while if the suspected LIFs are taken into account too, this rate yields a value of 3.35×10^{-7} meteoroids $\text{h}^{-1} \text{km}^{-2}$. These detection rates are at least two times higher than those of the aforementioned teams, which proves undoubtedly that NELIOTA has played a significant role in understanding the near-Earth meteoroid environment.

The temperature calculation is based on the assumption that LIFs emit as black bodies, which is also supported by spectroscopic observations (Yanagisawa et al. 2021; Yanagisawa & Kakinuma 2022). Therefore, although this is currently the only way for estimating the temperatures, future laboratory experiments provide a way to validate these estimates. The temperature calculation of LIFs is not straightforward and, except for the black body emission assumption, it depends also on the time resolution of the observing setup. As can be seen in Fig. B.1, all multiframe LIFs in both bands vanish faster in R than in the I passband. Obviously, this proves that they mostly emit in I , hence, our general impression that their vast majority are relatively cool is correct. The 39.6% of the validated flashes (76 out of 192) were detected in only one frame in R and in two frames in I band. That means that the emission in R lasted less than 33 ms (i.e., sum of the exposure and the readout time of one frame). Therefore, if we had used half of the frame rate (i.e., 15 fps) and the total exposure was 56 ms, we would have measured more photons in the I passband but the same in R . Thus, this would result in a lower peak temperature (i.e., higher $R - I$ index) that leads to an underestimation of the peak temperature. Therefore, thinking inversely, the higher the time resolution (higher frame rates) the more accurate the peak temperature estimation.

The time resolution also plays a significant role in the underestimation of the LE , and hence the E_{kin} , m_p , r_p , etc. In the case of single frame LIFs, we assume that all the luminous energy was emitted within the exposure time of the camera. However, it is likely that in some cases there was unrecorded LIF emission during the readout of the cameras, which leads to an underestimation of the meteoroid's mass. The calculation of the total energy flux of the multiframe LIFs, hence the corresponding meteoroid parameters, by using the energy correction method as described in Paper III, can be considered as more accurate, since only a small fraction of the emitted energy could be neglected (i.e., the LIF began to emit during the readout time before the first frame).

Constraining of the luminous efficiency η has proven to be a very difficult and tricky process, thus we preferred to perform our study based on its uncertainties. The η constraining can be achieved using only LIFs originating from stream meteoroid impacts (e.g., Moser et al. 2011), because their velocities are well determined from meteor showers. However, although this might sound easy, practically it is not. The first difficulty concerns the distinguishing between the stream and the sporadic meteoroids as shown by Ortiz et al. (2015) and Madiedo et al. (2015a,b). This distinction can be made only during a few days around the

maximum activity of the stream and probably only for the strong streams (i.e., those with high zenithal hourly rates) such as Perseids, Geminids, Lyrids, Taurids, Orionids, SDA. Except the narrow time window for observations for each stream, the subradiant point of the stream on Moon should be on its nightside. More specifically, the subradiant point should be ideally on the near-nightside of the Moon. If not, then it should be on its far-nightside or on its near-dayside in order for at least a small portion of the impact cone to be on the near-nightside. Moreover, according to the currently known observing setups of LIF observers, the illumination phase of the Moon should be less than 60% (for NELIOTA up to 45%) for the near-nightside to be observable (glare affect) and, in addition, its elevation should be appropriate for pointing the telescope. In all the aforementioned conditions, we should also add the weather constrains for a given observing site. However, another, and more important, difficulty concerns the meteoroid flux density distribution of the streams that varies from year to year for a given stream and it is not easily found either in the literature or online. Therefore, the combination of data of the same stream obtained in different years produces ambiguous results. We claim that in order to satisfy the above conditions, except the last one, the LIFs observers should increase around the globe in order to minimize the weather and elevation conditions constrains. For this, and as a first step, the NELIOTA team has developed and publicly released the Flash Detection Software (FDS⁸), which can be used from both amateurs and professional astronomers with a variety of equipment for the observations of LIFs. Regarding the meteoroid flux density of the streams, a unified network of ground based meteor stations that would provide the values for each stream seems to be the most appropriate direction of planning.

NELIOTA has significantly contributed to the studies of LIFs and the meteoroids. The observations ended in mid-August 2023 due to end of the funded program. The NELIOTA team plans to seek for new funding to re-initiate the operations. Observations of LIFs will continue using smaller size telescopes by other groups and hopefully amateur observers will join the effort using the FDS software. However, we argue that there is urgent need of a global LIF database establishment in order to host the data and distinguish the real LIF events from other false positives. We also highly recommend to establish a link between meteor, fireball, bolide and LIF observers for observations during meteor showers. The latter would certainly benefit the studies for the constraining of the luminous efficiency of the LIFs. We conclude that, although NELIOTA has gathered a sufficient sample of LIFs, a larger sample is needed, especially during the maximum activity of the meteoroid streams. Another promising direction for the future is observing in J -band during daytime (Sheward et al. 2023). Multiband observations with more than two filters are certainly desirable since they will provide better estimation of the emitted luminous energy. More sensitive (e.g., quantum efficiency >80-90%), higher speed (e.g., 100-200 fps) cameras with shorter readout times (e.g., 1-2 ms) on multiband (e.g., two or more passbands) beam splitters attached to meter size telescopes will allow for a better time resolution of the LIFs, hence for a better estimation of their peak temperatures. All these steps are recommended to take place in the following 2-3 years before the planned launch of the 'Lunar Meteoroid Impact Observer' (LUMIO) mission⁹ (Topputo et al. 2018; Cipriano et al. 2018; Topputo et al. 2023) in 2026. LUMIO, similar to the NE-

⁸ <https://kryoneri.astro.noa.gr/en/flash-detection-software/>

⁹ <https://www.eoportal.org/satellite-missions/lumio>

LIIOTA setup, will be equipped with two cameras attached to a dichroic beam splitter and will observe in the visible and near infrared bands with a frame rate of 15-20 fps. It will continuously observe the Moon for approximately 15 days per month, when lunar illumination phase is less than 50%. Even though LUMIO is anticipated to observe hundreds of LIFs, its position at the Earth-Moon L2 area cannot permanently solve the aforementioned problem with the subradiant point of a stream on the Moon. Moreover, due to the opposition of the spacecraft with respect to Earth, it will observe the Moon at opposite phases than the observers on Earth. Therefore, we argue that ground based observations from various sites should continue as they are complementary to those of LUMIO.

8. Summary and conclusions

This work presented detailed results for 113 validated and 70 suspected lunar impact flashes observed by NELIOTA between August 2019 and mid-August 2023. From this sample, 99 were multiframe flashes and their light curves were presented. From the latter LIFs, 15 of them were multiframe flashes in both passbands, hence, their temperature curves were presented as well. Physical properties of the impacting meteoroids, temperatures of the impacts and expected crater sizes were calculated for these events. These results were combined with the previous of the NELIOTA team (Paper III) yielding a total sample of 192 validated and 103 suspected LIFs observed during a total of 283.4 h between February 2017 - mid-August 2023. An extensive statistical analysis was presented regarding the properties of the projectiles and their impacts on Moon as well as their appearance frequencies on Moon and around Earth. These frequencies were further used to estimate the impact probabilities of a meteoroid, lying within specific physical properties ranges, with a hypothetical lunar infrastructure or with an orbiting satellite. The statistics of the energies of the projectiles were compared with known catastrophic energies in order to estimate the possible damage on a space vehicle or building.

Using the recommended values of luminous efficiency η , we derived the statistics of the masses and the radii of the impacting meteoroids produced validated LIFs. For the suspected LIFs, we made rough estimation of the meteoroid parameters based on the LE per band correlation as yielded from the validated LIFs. Our statistics, for $\eta = 1.5 \times 10^{-3}$, showed that the majority (75-80%) of the impacting meteoroids that produced validated LIFs have masses less than 200 g and radii less than 3 cm (i.e., smaller than a tennis ball) and produced craters with sizes between 1.5-3 m. Empirical relations between the magnitudes of the LIFs in each observed band and the meteoroid masses were derived for various meteoroid velocities.

The vast majority ($\sim 85\%$) of the impacts produced peak temperatures within the range 2000-4500 K confirming that they are relatively cool events. However, no clear correlation between the temperature and the mass or the size of the meteoroids was found. Moreover, for the multiframe LIFs in both passbands, we found that there is no unique behaviour after the observed maximum temperature, meaning that most of them exhibit a drop off after the peak, but many of them presented constant or a slight increase in temperature. These results indicate that melting and/or complicated thermal processes of the plume probably play a significant role to the thermal evolution and the peak temperature.

The appearance frequency of meteoroids around Earth and on Moon, based on the NELIOTA LIF detection rates, allowed for the estimation of the probability of a potential impact of a meteoroid with a hypothetical infrastructure on Moon (e.g., lunar

bases) or with a satellite. It should be clarified that the calculated probabilities concern only meteoroids with the aforementioned physical properties (i.e., a few grams up to several hundreds of grams and sizes of the order of a few centimeters) and not their global population (e.g., micro- or nano- meteoroids). The impact probability is directly proportional to the potential impact surface area and the duration of the mission. Small buildings on Moon (e.g., with surface areas less than 400 m²) have tiny probabilities of being hit ($2 - 9 \times 10^{-5}$) even within a 10-year time period. However, for larger buildings (surface ~ 8000 m²) or group of buildings (dependent of each other) the probability increases and reaches the value of 0.9% in the extreme scenario (based on validated and suspected LIFs during streams). More or less, the same stands for the orbiting satellites. The larger the surface area of the panels or the spacecraft itself the higher the impact probability. For small size satellites (e.g., Starlink size or cubeSats) the impact probability is extremely low (order of 10^{-7}) for a mission duration of five years, but reaches the 1-2% for International Space Station sizes for longer periods of time. On the other hand, although these probabilities seem very low, the damages that can be caused may be catastrophic for the missions, since the transferred energy of the meteoroids could reach the order of 1 GJ (i.e., similar to hand grenade explosion), but typically is of the order of 10-100 MJ (i.e., energy released by fireworks). Undoubtedly, along with the estimated probability of a meteoroid impact, the latter should be taken into account by the space industry for the shielding of space vehicles of buildings.

Acknowledgements. The authors gratefully acknowledge financial support by the European Space Agency under the NELIOTA program (up to January 2021), contract No. 4000112943, and the Consolidating Activities Regarding Moon, Earth and NEOs (CARMEN) project (August 2021-July 2023), No. 4000134667, via a subcontract of NOA with 6ROADS. The observations of August 2023 were funded by Europlanet 2024 RI after a successful telescope time application by D. V. K., A. L., and A. Z. B. Europlanet 2024 RI has received funding from the European Union's Horizon 2020 research and innovation programme under grant agreement No 871149. The authors wish to thank the referee M. Yanagisawa for his fruitful comments that improved the quality of the paper. This study is based on observations made with the 1.2 m Kryoneri telescope, Corinthia, Greece, which is operated by the Institute for Astronomy, Astrophysics, Space Applications and Remote Sensing of the National Observatory of Athens, Greece.

References

- Avdellidou, C., Munaibari, E., Larson, R., et al. 2021, *Planet. Space Sci.*, 200, 105201
- Avdellidou, C. & Vaubaillon, J. 2019, *MNRAS*, 484, 5212
- Babadzhanov, P. B. & Kokhirova, G. I. 2009, *A&A*, 495, 353
- Bellot Rubio, L. R., Ortiz, J. L., & Sada, P. V. 2000a, *ApJ*, 542, L65
- Bellot Rubio, L. R., Ortiz, J. L., & Sada, P. V. 2000b, *Earth Moon and Planets*, 82, 575
- Bonanos, A. Z., Avdellidou, C., Liakos, A., et al. 2018, *A&A*, 612, A76
- Bouley, S., Baratoux, D., Vaubaillon, J., et al. 2012, *Icarus*, 218, 115
- Brown, P., Wong, D. K., Weryk, R. J., & Wiegert, P. 2010, *Icarus*, 207, 66
- Cipriano, A. M., Dei Tos, D. A., & Topputo, F. 2018, *Frontiers in Astronomy and Space Sciences*, 5, 29
- Gault, D. E. 1974, in *A Primer in Lunar Geology*, ed. R. Greeley & P. H. Schultz
- Liakos, A., Bonanos, A., Xilouris, E., et al. 2019, in *1st NEO and Debris Detection Conference_ESA2019*, 20
- Liakos, A., Bonanos, A. Z., Xilouris, E. M., et al. 2020, *A&A*, 633, A112
- Madiedo, J. M., Ortiz, J. L., & Morales, N. 2017, in *Lunar and Planetary Science Conference*, 1319
- Madiedo, J. M., Ortiz, J. L., & Morales, N. 2018, *MNRAS*, 480, 5010
- Madiedo, J. M., Ortiz, J. L., Morales, N., & Cabrera-Caño, J. 2015a, *Planet. Space Sci.*, 111, 105
- Madiedo, J. M., Ortiz, J. L., Morales, N., Roman, A., & Alonso, S. 2019, in *Lunar and Planetary Science Conference*, Lunar and Planetary Science Conference, 1406
- Madiedo, J. M., Ortiz, J. L., Organero, F., et al. 2015b, *A&A*, 577, A118

- Melosh, H. J. 1989, *Impact cratering: A geologic process* (Oxford University Press)
- Moser, D. E., Suggs, R. M., Swift, W. R., et al. 2011, in *Meteoroids: The Smallest Solar System Bodies*, ed. W. J. Cooke, D. E. Moser, B. F. Hardin, & D. Janches, 142
- Munaibari, E., Larson, R., Avdellidou, C., et al. 2020, in *European Planetary Science Congress, EPSC2020–728*
- Ortiz, J. L., Aceituno, F. J., Quesada, J. A., et al. 2006, *Icarus*, 184, 319
- Ortiz, J. L., Madiedo, J. M., Morales, N., Santos-Sanz, P., & Aceituno, F. J. 2015, *MNRAS*, 454, 344
- Rembold, J. J. & Ryan, E. V. 2015, *Planet. Space Sci.*, 117, 119
- Sheward, D., Delbo, M., Avdellidou, C., et al. 2023, *MNRAS*[arXiv:2308.00510]
- Suggs, R. M., Moser, D. E., Cooke, W. J., & Suggs, R. J. 2014, *Icarus*, 238, 23
- Swift, W. R., Moser, D. E., Suggs, R. M., & Cooke, W. J. 2011, in *Meteoroids: The Smallest Solar System Bodies*, ed. W. J. Cooke, D. E. Moser, B. F. Hardin, & D. Janches, 125
- Topputo, F., Dei Tos, D. A., & Cipriano, A. 2018, in *42nd COSPAR Scientific Assembly, Vol. 42, PSD.1–28–18*
- Topputo, F., Merisio, G., Franzese, V., et al. 2023, *Icarus*, 389, 115213
- Xilouris, E. M., Bonanos, A. Z., Bellas-Velidis, I., et al. 2018, *A&A*, 619, A141
- Yanagisawa, M. & Kakinuma, F. 2022, *Earth, Planets and Space*, 74, 62
- Yanagisawa, M., Uchida, Y., Kurihara, S., et al. 2021, *Planet. Space Sci.*, 195, 105131

Appendix A: Tables of results

Appendix B: Multiframe flashes

In this appendix, we provide the magnitude values for all the multiframe flashes (Table B.1). For flashes with more than two set of frames in *R* and *I* bands, the corresponding temperature of each set of frames is also given. Moreover, the light curves of these flashes are plotted in Fig. B.1 and the temperature evolution curves in Fig. B.2.

Appendix C: Stream and sporadic meteoroid parameters

Appendix D: Extra figures

Table A. 1: Photometric results and locations of the detected flashes by NELIOTA after July 2019. Errors are included in parentheses alongside magnitude values and correspond to the last digit(s). The error in the determination of the location is set as 0.5°.

ID	Date & UT	Val.	t_{\max} (ms)	m_R (mag)	m_I (mag)	Lat. (°)	Long. (°)	ID	Date & UT	Val.	t_{\max} (ms)	m_R (mag)	m_I (mag)	Lat. (°)	Long. (°)
113	2019 08 06 18:08:34.853	SC2	33	10.15(12)	9.81(15)	10.3	-69.2	155	2020 07 25 18:55:58.669	SC2	33	10.20(12)	9.38(10)	6.5	-78.1
114	2019 08 06 18:19:16.023	Val.	66	10.37(28)	8.71(12)	18.7	-26.3	156	2020 07 26 19:08:21.285	Val.	33	10.20(12)	9.13(12)	14.0	-28.6
115 ^a	2019 08 06 18:50:01.718	SC2	66	8.49(11)	8.35(10)	18.3	-21.2	157	2020 07 26 19:10:25.428	Val.	66	9.15(10)	7.82(6)	11.3	-35.2
116	2019 08 06 18:56:36.990	Val.	66	8.43(12)	7.38(7)	23.0	-7.3	158	2020 08 13 00:57:10.702	Val.	33	10.16(26)	9.03(9)	2.3	40.9
117	2019 08 06 18:59:15.735	Val.	33	9.34(13)	9.00(9)	41.0	-56.0	159	2020 08 14 00:54:21.133	Val.	33	9.29(15)	8.53(9)	-12.0	35.7
118	2019 08 26 02:50:56.348	Val.	66	10.65(27)	10.11(7)	9.1	42.7	160	2020 08 14 01:15:36.278	Val.	66	9.95(20)	9.45(12)	18.0	20.6
119 ^a	2019 08 27 02:58:28.586	SC2	33	10.44(17)	10.29(12)	-33.5	40.8	161	2020 12 09 03:09:58.098	Val.	33	9.83(18)	9.32(10)	0.4	78.1
120	2019 08 28 03:03:30.931	Val.	33	10.98(31)	9.82(16)	-17.2	33.9	162	2021 03 17 17:46:52.983	Val.	99	9.48(12)	7.97(6)	-25.8	-12.3
121	2019 09 05 18:11:59.277	Val.	33	10.13(21)	9.52(11)	-22.5	-65.9	163	2021 03 17 18:03:02.205	SC1	66	10.14(15)	10.14(15)	-20.1	-69.0
122	2019 09 05 18:51:32.998	Val.	33	10.25(27)	9.53(16)	-4.8	-53.0	164	2021 03 17 18:07:18.604	Val.	33	10.47(22)	9.21(8)	28.1	-28.7
123	2019 09 23 01:08:44.025	SC2	33	10.20(28)	9.40(11)	3.0	66.9	165	2021 04 18 19:13:58.703	Val.	99	9.43(15)	7.89(6)	17.2	-55.6
124	2019 09 23 03:36:21.556	Val.	66	8.43(8)	7.42(5)	-31.8	25.6	166	2021 04 18 19:24:00.000	Val.	33	9.74(20)	8.64(10)	-19.6	-35.6
125	2019 09 25 03:40:11.073	Val.	99	8.43(8)	7.42(5)	12.5	17.8	167	2021 05 15 18:38:40.847	Val.	33	10.12(22)	9.38(10)	0.3	-15.7
126	2019 10 22 04:11:36.271	Val.	66	10.00(18)	9.28(11)	-1.6	65.3	168	2021 05 18 20:08:21.742	Val.	66	9.90(20)	8.66(7)	-6.0	-57.2
127	2019 10 24 02:30:16.186	Val.	66	9.49(15)	7.88(7)	-5.7	55.0	169	2021 06 15 19:06:12.914	Val.	66	9.96(15)	9.19(8)	-3.6	-44.5
128	2019 10 25 03:43:44.133	SC2	33	10.78(20)	10.78(20)	12.0	22.5	170	2021 06 15 19:15:27.433	SC1	66	10.86(32)	10.19(17)	2.4	-43.7
129	2019 11 02 16:20:44.065	SC1	66	10.22(29)	9.26(12)	9.9	-26.1	171	2021 06 15 19:23:18.620	Val.	66	8.15(10)	6.73(6)	22.5	-78.8
130	2019 11 02 17:19:19.668	Val.	66	10.22(29)	9.26(12)	-33.9	-48.3	172	2021 06 15 19:38:52.236	Val.	165	10.82(18)	10.33(17)	-11.3	82.1
131	2019 11 03 17:49:38.486	Val.	33	9.61(23)	8.77(12)	12.1	-25.3	173	2021 07 03 01:23:35.666	SC1	66	9.26(12)	9.26(12)	3.3	66.8
132	2019 11 03 16:14:30.209	Val.	33	9.17(15)	8.46(12)	-16.7	3.3	174	2021 07 05 01:48:25.878	SC2	33	9.81(17)	9.81(17)	11.3	26.6
133	2019 12 01 16:23:13.796	Val.	132	8.42(10)	5.57(7)	-13.1	-23.1	175	2021 07 06 02:11:11.359	Val.	33	10.20(27)	8.76(9)	13.9	-43.4
134	2019 12 01 16:30:43.411	Val.	33	10.75(28)	9.12(15)	16.5	-40.7	176	2021 07 15 19:22:29.410	Val.	33	9.96(34)	9.15(12)	3.1	-34.9
135	2019 12 01 17:14:41.437	Val.	33	11.16(39)	9.35(15)	-28.6	-32.4	177	2021 07 16 18:49:32.113	Val.	66	9.55(21)	9.46(15)	22.1	24.5
136	2019 12 20 04:34:16.679	Val.	99	9.50(20)	8.51(7)	-39.8	48.7	178 ^a	2021 08 02 00:48:25.336	SC2	33	10.41(29)	9.85(14)	4.4	80.2
137 ^b	2020 01 30 17:17:59.771	SC2	165	10.35(21)	10.07(15)	23.1	-40.8	179	2021 08 02 01:26:06.111	Val.	66	8.75(18)	8.28(9)	4.8	30.3
138	2020 01 30 17:18:08.539	Val.	66	11.03(33)	9.51(12)	21.9	-46.5	180	2021 08 02 01:34:28.145	Val.	66	10.12(26)	9.72(15)	-4.8	52.8
139	2020 01 30 17:35:38.892	Val.	33	10.62(22)	9.75(12)	-39.1	-40.4	181	2021 08 02 02:44:36.306	Val.	66	8.85(17)	7.74(6)	28.4	16.3
140	2020 01 30 18:53:24.062	SC2	33	10.62(22)	9.75(12)	-29.9	-72.8	182	2021 08 02 02:51:02.646	Val.	99	10.16(19)	9.37(9)	-34.7	33.9
141	2020 01 31 17:37:21.034	SC2	33	10.62(22)	9.75(12)	-29.9	-72.8	183	2021 10 03 03:14:17.079	Val.	33	8.66(13)	7.73(8)	-21.2	-71.8
142	2020 03 01 16:54:23.862	Val.	99	8.32(8)	7.15(4)	-7.8	-45.1	184	2021 10 11 16:57:00.374	Val.	165	9.33(22)	8.25(10)	-15.1	-32.5
143	2020 03 01 17:10:06.375	Val.	33	9.92(25)	9.42(12)	-30.6	-31.3	185	2021 10 12 16:31:15.618	Val.	66	9.75(20)	8.75(10)	11.2	-77.3
144	2020 03 27 17:40:25.320	Val.	66	10.01(15)	8.70(8)	-1.9	-32.1	186	2021 10 12 17:42:17.599	Val.	66	8.58(12)	10.00(13)	-30.6	73.8
145	2020 03 29 18:14:10.875	Val.	66	10.83(23)	9.72(9)	15.1	-91.3	187	2021 12 01 04:21:42.906	SC1	66	10.17(31)	8.20(8)	14.1	-56.0
146	2020 03 29 19:07:30.900	SC2	33	10.18(21)	10.00(14)	0.4	-59.5	188	2021 12 08 16:15:10.805	Val.	66	8.87(17)	7.53(6)	4.7	-15.4
147	2020 03 29 19:16:46.509	Val.	33	10.18(21)	9.26(9)	-22.7	-42.8	189	2021 12 08 16:34:21.521	Val.	33	9.31(15)	7.95(7)	-7.8	-43.2
148	2020 04 28 19:19:54.525	Val.	66	8.99(10)	8.13(5)	-26.6	-47.7	190	2022 02 05 17:41:56.145	SC2	33	8.87(17)	7.53(6)	4.7	-15.4
149 ^a	2020 06 15 02:04:12.513	SC2	33	9.50(19)	9.34(12)	49.4	58.0	191	2022 04 05 17:30:55.889	Val.	99	8.87(17)	7.53(6)	4.7	-15.4
150	2020 06 16 02:09:14.848	SC1	66	7.92(10)	9.53(13)	-10.7	67.2	192	2022 04 05 17:54:37.532	Val.	33	9.31(15)	7.95(7)	-7.8	-43.2
151	2020 06 25 18:28:18.340	Val.	132	7.92(10)	6.66(6)	10.8	-46.5	193	2022 05 07 20:47:14.061	SC1	66	7.41(8)	7.41(8)	8.8	-34.4
152	2020 06 25 19:09:24.063	SC1	66	9.76(13)	9.76(13)	33.4	-33.1	194	2022 05 25 02:25:10.955	SC2	33	7.96(11)	6.64(6)	-4.0	-28.8
153	2020 06 26 19:52:31.569	Val.	66	9.73(11)	8.22(7)	12.7	-24.9	195	2022 06 03 18:21:31.378	Val.	132	7.96(11)	6.64(6)	-4.0	-28.8
154	2020 07 25 18:41:34.204	SC2	33	9.61(13)	9.61(13)	17.3	-30.0	196	2022 06 03 18:57:25.884	SC1	66	9.17(9)	9.17(9)	35.8	-29.5

Notes. Val.= Validated flash, SC1/2 = Suspected flash of Class 1/2 (see Paper III for details), ^(a) abnormal R-I index, ^(b) slight displacement and abnormal temperature evolution.

Table A.1 (cont'd)

ID	Date & UT	Val.	t_{\max} (ms)	m_R (mag)	m_I (mag)	Lat. ($^{\circ}$)	Long. ($^{\circ}$)	ID	Date & UT	Val.	t_{\max} (ms)	m_R (mag)	m_I (mag)	Lat. ($^{\circ}$)	Long. ($^{\circ}$)	
197	2022 06 03 19:21:10.176	SC2	33		8.64(9)	-5.0	-22.8	239	2022 10 30 16:42:35.356	SC2	33	10.16(22)	10.16(22)	24.8	-53.1	
198	2022 06 03 19:34:16.804	SC1	66		9.44(13)	-9.4	-75.9	240	2022 10 30 16:47:27.612	Val.	66	9.68(22)	8.56(9)	-1.3	-75.6	
199	2022 06 04 18:20:50.612	Val.	66	9.40(28)	8.32(9)	-7.2	-25.0	241	2022 10 30 16:54:54.929	Val.	66	9.65(19)	8.57(9)	-27.6	-59.0	
200	2022 06 04 18:22:46.921	Val.	33	10.15(38)	9.19(14)	16.2	-19.9	242	2022 10 30 17:13:28.165	SC1	66		8.98(14)	-7.6	-21.1	
201	2022 06 04 19:44:16.807	Val.	33	10.06(31)	9.45(15)	-9.4	-59.7	243	2022 10 30 17:34:04.033	SC2	33		9.44(15)	4.1	-51.0	
202	2022 06 23 01:46:07.604	Val.	66	8.73(15)	7.22(7)	5.3	84.4	244	2022 10 30 17:34:16.134	Val.	132	8.64(14)	8.03(11)	-18.9	-45.2	
203 ^c	2022 07 22 00:27:39.090	SC2	33	9.21(25)	8.84(17)	-7.3	24.6	245	2022 10 30 17:41:51.409	SC1	66		8.98(13)	-26.8	-46.3	
204	2022 07 22 02:13:27.207	Val.	66	9.97(24)	8.73(7)	-4.6	57.1	246	2022 10 30 18:06:20.288	SC2	33		9.50(18)	10.5	-48.4	
205	2022 07 22 02:48:11.224	Val.	66	10.27(36)	9.29(14)	10.7	51.1	247	2022 10 30 18:11:38.346	SC2	33		9.02(15)	13.9	-57.9	
206	2022 07 22 02:49:51.365	Val.	132	9.36(29)	7.51(10)	13.1	12.7	248	2022 10 30 18:13:57.723	SC2	33		9.53(18)	17.3	-88.0	
207	2022 07 24 02:23:51.582	SC2	33		9.95(11)	23.9	44.4	249	2022 10 31 18:58:46.938	SC2	33		8.92(13)	-5.2	-79.1	
208	2022 08 01 18:27:23.335	Val.	33	9.93(27)	8.66(15)	6.9	-45.3	250	2022 10 31 19:17:17.423	Val.	66	8.60(21)	7.51(12)	7.1	-35.2	
209	2022 08 01 18:28:18.506	Val.	99	9.42(21)	8.66(9)	-4.1	-75.7	251	2022 11 19 02:39:27.785	Val.	66	8.82(15)	7.92(8)	-13.6	21.6	
210	2022 08 03 18:05:38.820	SC1	66		8.66(9)	-4.1	-75.7	252	2022 11 19 02:45:43.608	SC1	66		8.51(10)	-3.4	21.6	
211	2022 08 03 18:17:31.174	SC2	33		9.42(13)	10.8	-55.5	253	2022 11 19 03:51:52.914	SC2	33		9.48(14)	-2.4	40.9	
212	2022 08 03 18:23:42.636	Val.	66	9.76(12)	8.37(8)	28.5	-73.1	254	2022 11 19 04:05:36.877	SC2	33		9.42(13)	-1.3	69.3	
213	2022 08 03 19:02:12.594	SC1	66		10.04(19)	-4.1	-86.4	255	2022 11 19 04:15:39.560	SC2	33		8.77(9)	9.5	30.0	
214	2022 08 04 18:47:06.667	Val.	66	9.26(18)	7.63(13)	-21.0	-40.7	256	2022 12 18 03:37:48.471	Val.	66	9.11(14)	7.73(6)	-2.2	51.7	
215	2022 08 04 19:24:20.958	SC1	66		8.02(12)	-4.2	-67.1	257	2022 12 18 03:47:47.156	Val.	66		9.93(20)	2.6	72.5	
216	2022 08 04 19:25:11.729	SC1	66		9.40(19)	6.7	-73.5	258	2022 12 26 15:46:16.570	Val.	198	7.76(11)	6.38(8)	-15.9	-53.2	
217	2022 08 22 01:33:02.291	SC1	66		8.45(9)	-17.7	8.0	259	2022 12 26 16:38:05.663	SC2	33		10.45(21)	2.2	-29.3	
218	2022 08 22 02:11:20.544	SC2	33		9.86(26)	-14.1	89.1	260	2022 12 26 16:48:14.320	Val.	66	10.26(20)	9.68(12)	0.2	-66.5	
219	2022 09 01 18:33:36.493	Val.	66	10.66(37)	8.04(14)	17.9	-62.0	261	2022 12 27 16:18:50.350	Val.	33	9.64(22)	9.08(12)	-11.4	-8.0	
220	2022 09 02 18:06:48.349	SC2	33		9.36(15)	33.7	-34.1	262	2022 12 27 17:42:53.269	SC2	66		8.84(16)	8.71(11)	12.4	-11.4
221	2022 09 02 19:03:02.542	SC2	33		8.36(15)	10.2	-22.8	263 ^u	2022 12 27 17:47:37.390	Val.	66	9.29(17)	7.98(9)	-7.2	-11.2	
222	2022 10 19 01:43:11.699	SC1	66		9.88(15)	-9.1	79.8	264	2022 12 27 17:57:38.537	SC2	33		9.81(16)	-13.6	-46.8	
223	2022 10 19 03:03:44.141	Val.	99	8.47(10)	8.25(6)	-3.3	61.6	265	2022 12 27 18:11:32.401	Val.	66	9.73(12)	8.53(13)	-29.6	-6.6	
224	2022 10 20 01:12:58.151	Val.	429	8.58(14)	7.38(8)	-14.2	21.4	266	2023 01 16 04:11:21.224	Val.	66	10.09(26)	9.04(9)	-36.9	51.7	
225	2022 10 20 01:23:08.098	SC2	33		9.89(14)	-7.5	53.8	267	2023 02 22 17:49:40.667	Val.	33	10.37(22)	10.15(16)	-41.0	-32.0	
226	2022 10 20 02:05:55.914	SC1	66		9.14(9)	6.3	50.0	268	2023 02 22 17:52:04.312	Val.	99	9.97(19)	8.70(13)	-33.4	-16.7	
227	2022 10 20 02:56:37.878	Val.	66	9.08(10)	8.59(6)	-7.2	87.3	269	2023 02 24 17:25:21.560	SC1	66		10.00(13)	2.1	-62.2	
228	2022 10 20 03:32:21.841	SC2	33		9.83(14)	0.6	74.8	270	2023 03 24 18:36:01.406	SC2	33		10.24(15)	-14.4	-53.0	
229	2022 10 20 04:11:08.419	SC1	66		8.90(8)	-14.9	70.1	271	2023 03 26 20:25:28.546	Val.	66	9.88(18)	8.79(10)	18.4	-72.5	
230	2022 10 21 02:55:11.697	Val.	66	10.22(24)	9.56(10)	-2.9	68.0	272	2023 03 27 17:23:31.571	SC2	33		9.70(11)	20.9	-55.4	
231	2022 10 22 03:07:56.784	Val.	33	10.92(28)	10.27(15)	-26.1	59.6	273	2023 03 27 18:25:58.056	SC2	33		8.74(7)	-2.1	-38.3	
232	2022 10 22 03:25:17.830	Val.	33	10.44(10)	9.55(13)	-21.8	21.0	274	2023 04 23 18:04:39.828	Val.	66	10.60(23)	9.61(10)	20.04	-20.5	
233	2022 10 22 03:39:55.152	Val.	33	10.70(15)	9.91(7)	-26.4	22.9	275	2023 04 24 17:58:30.793	Val.	33	10.47(32)	9.10(8)	-28.9	-26.5	
234	2022 10 22 03:55:35.517	Val.	66	9.51(14)	8.68(7)	-25.0	49.2	276	2023 04 24 19:54:33.094	SC2	33		9.71(14)	-5.5	-33.0	
235	2022 10 22 03:56:50.322	Val.	66	10.31(25)	9.51(11)	-4.7	14.8	277	2023 04 24 19:58:40.780	SC2	33		10.08(18)	-3.9	-54.8	
236	2022 10 29 17:03:58.478	Val.	99	9.25(19)	7.72(13)	-7.7	-65.2	278	2023 04 24 20:02:42.098	Val.	66	9.63(25)	8.28(10)	-26.36	-32.3	
237	2022 10 29 17:13:31.322	SC1	66		7.68(13)	4.5	-53.0	279	2023 05 23 20:06:14.792	Val.	66	8.94(16)	8.16(11)	-12.03	-12.9	
238	2022 10 30 16:41:05.648	Val.	33	10.08(30)	9.26(14)	-16.9	-25.9	280								

Notes. Val.= Validated flash, SC1/2 = Suspected flash of Class 1/2 (see Paper III for details), ^(a) abnormal R-I index, ^(b) slight displacement and abnormal temperature evolution, ^(c) too elongated shape in I filter and too short duration for its magnitude.

Table A.1 (cont'd)

ID	Date & UT	Val.	t_{\max} (ms)	m_R (mag)	m_I (mag)	Lat. ($^{\circ}$)	Long. ($^{\circ}$)	ID	Date & UT	Val.	t_{\max} (ms)	m_R (mag)	m_I (mag)	Lat. ($^{\circ}$)	Long. ($^{\circ}$)
281	2023 05 24 20:11:10.028	Val.	330	8.32(11)	6.41(8)	23.3	-67.3	289	2023 08 10 01:53:23.822	Val.	66	9.67(16)	8.50(6)	17.2	69.3
282	2023 05 24 21:03:20.168	Val.	132	9.10(18)	7.53(13)	10.9	-36.1	290	2023 08 11 01:43:53.825	Val.	66	11.32(41)	9.94(14)	37.3	71.6
283	2023 05 25 20:34:27.999	Val.	231	7.51(10)	6.28(7)	-5.9	-82.9	291	2023 08 11 02:53:30.790	SC1	66		9.28(13)	36.9	13.6
284	2023 05 26 18:17:43.624	Val.	66	9.79(38)	8.25(9)	0.16	-24.5	292	2023 08 13 02:29:01.918	Val.	33	11.65(65)	10.07(13)	22.3	19.6
285	2023 06 21 18:47:44.161	Val.	33	9.21(12)	9.00(9)	20.4	-45.4	293	2023 08 13 02:33:29.605	Val.	33	10.59(29)	10.04(11)	16.8	83.8
286	2023 06 22 19:58:08.964	Val.	33	11.00(36)	10.24(17)	-3.0	-79.0	294	2023 08 13 02:57:22.550	SC2	33		11.30(33)	-6.1	51.0
287	2023 06 22 20:03:20.188	Val.	99	10.18(20)	8.53(12)	45.7	-79.2	295	2023 08 13 03:05:54.033	Val.	66	9.30(13)	8.76(8)	23.5	49.8
288	2023 06 22 20:11:59.394	SC2	33		10.23(21)	-24.6	-44.7								

Notes. Val.= Validated flash, SC1/2 = Suspected flash of Class 1/2 (see Paper III for details), ^(a) abnormal $R - I$ index, ^(b) slight displacement and abnormal temperature evolution, ^(c) too elongated shape in I filter and too short duration for its magnitude.

Table A.2: Results for the validated flashes detected by the NELIOTA campaign between August 2019 and mid-August 2023 as well as for the corresponding projectiles and craters for various η values. Errors are included in parentheses alongside values and correspond to the last digit(s).

ID	Stream	$\eta = 5 \times 10^{-3}$						$\eta = 1.5 \times 10^{-3}$						$\eta = 5 \times 10^{-4}$					
		LE_R ($\times 10^4$ J)	LE_I ($\times 10^4$ J)	T (K)	KE_p ($\times 10^6$ J)	m_p (g)	r_p (cm)	d_c (m)	KE_p ($\times 10^6$ J)	m_p (g)	r_p (cm)	d_c (m)	KE_p ($\times 10^6$ J)	m_p (g)	r_p (cm)	d_c (m)	KE_p ($\times 10^6$ J)	m_p (g)	r_p (cm)
114	PER	0.5(1)	1.6(1)	2237(317)	4.2(4)	2.3(2)	0.8(1)	1.39(5)	14(1)	8(1)	1.1(1)	2.0(1)	42(4)	23(2)	1.6(0.2)	2.7(1)			
116	PER	2.9(3)	5.3(3)	3151(305)	16.3(8)	8.8(4)	1.2(1)	2.07(6)	54(3)	29(1)	1.8(2)	2.9(1)	163(8)	88(4)	2.6(0.3)	4.0(1)			
117	PER	1.3(2)	0.9(1)	6149(1410)	4.2(3)	2.3(2)	0.8(1)	1.40(5)	14(1)	8(1)	1.1(1)	2.0(1)	42(3)	23(2)	1.6(0.2)	2.7(1)			
118	spo	0.4(1)	1.5(1)	2933(600)	3.8(2)	26.3(1.5)	1.5(5)	1.45(5)	13(1)	88(5)	2.2(7)	2.1(1)	38(2)	263(15)	3.2(1.1)	2.8(1)			
120	spo	0.3(1)	0.4(1)	2933(600)	1.3(2)	9.2(1.4)	1.1(3)	1.07(5)	4(1)	31(5)	1.6(5)	1.5(1)	13(2)	92(14)	2.3(0.8)	2.1(1)			
121	spo	0.6(1)	0.6(1)	4443(1207)	2.3(3)	16.2(1.8)	1.3(4)	1.26(5)	8(1)	54(6)	1.9(6)	1.8(1)	23(3)	162(18)	2.8(0.9)	2.5(1)			
122	spo	0.5(1)	0.6(1)	4016(1214)	2.2(3)	15.2(2.2)	1.3(4)	1.24(6)	7(1)	51(7)	1.9(6)	1.8(1)	22(3)	152(22)	2.7(0.9)	2.4(1)			
124	spo	0.6(1)	1.2(1)	3777(1042)	3.5(3)	24.4(2.4)	1.5(5)	1.42(6)	12(1)	81(8)	2.2(7)	2.0(1)	35(3)	244(24)	3.2(1.0)	2.8(1)			
125	spo	4.1(2)	5.7(2)	3212(207)	19.6(6)	135.8(3.8)	2.6(8)	2.33(7)	65(2)	453(13)	4(1)	3.3(1)	196(6)	1358(38)	5.6(1.8)	4.5(1)			
126	spo	0.7(1)	1.1(1)	4036(810)	3.6(3)	25.1(2.0)	1.5(5)	1.43(5)	12(1)	84(7)	2.2(7)	2.0(1)	36(3)	251(20)	3.2(1.0)	2.8(1)			
127	spo	1.1(1)	3.4(2)	2288(160)	9.0(4)	62.6(3.0)	2.0(7)	1.86(6)	30(1)	209(10)	3(1)	2.6(1)	90(4)	626(30)	4.3(1.4)	3.6(1)			
130	spo	0.5(1)	1.3(1)	3345(770)	3.7(4)	25.5(2.5)	1.5(5)	1.43(6)	12(1)	85(8)	2.2(7)	2.0(1)	37(4)	255(25)	3.2(1.1)	2.8(1)			
131	spo	0.9(2)	1.2(1)	3641(770)	4.3(5)	29.7(3.3)	1.6(5)	1.50(6)	14(2)	99(11)	2.3(8)	2.1(1)	43(5)	297(33)	3.4(1.1)	2.9(1)			
132	spo	1.4(2)	1.6(2)	4080(647)	6.0(5)	41.3(3.7)	1.8(6)	1.65(6)	20(2)	138(12)	2.6(9)	2.3(1)	60(5)	413(37)	3.7(1.2)	3.2(1)			
133	spo	4.6(3)	34.8(1.6)	1438(53)	79(3)	544.8(22.7)	4(1)	3.49(1.1)	262(11)	1816(76)	6(2)	4.9(1)	787(33)	5448(227)	8.8(2.9)	6.8(2)			
134	spo	0.4(1)	0.9(1)	2277(353)	2.5(3)	17.3(2.1)	1.3(4)	1.28(6)	8(1)	58(7)	2.0(6)	1.8(1)	25(3)	173(21)	2.8(0.9)	2.5(1)			
135	spo	0.3(1)	0.7(1)	2093(363)	2.0(3)	13.5(1.9)	1.2(4)	1.19(6)	7(1)	45(6)	1.8(6)	1.7(1)	20(3)	135(19)	2.6(0.9)	2.3(1)			
136	spo	1.2(2)	3.1(1)	3254(477)	8.7(5)	60.2(3.6)	2.0(6)	1.84(6)	29(2)	201(12)	3(1)	2.6(1)	87(5)	602(36)	4.2(1.4)	3.6(1)			
138	spo	0.3(1)	1.4(1)	2393(427)	3.4(3)	23.5(1.7)	1.5(5)	1.40(5)	11(1)	78(6)	2.2(7)	2.0(1)	34(3)	235(17)	3.1(1.0)	2.7(1)			
139	spo	0.4(1)	0.5(1)	3558(727)	1.9(2)	13.2(1.5)	1.2(4)	1.19(5)	6(1)	44(5)	1.8(6)	1.7(1)	19(2)	132(15)	2.6(0.8)	2.3(1)			
142	spo	3.7(3)	8.9(2)	2919(161)	25.3(7)	175.4(4.9)	2.8(9)	2.51(7)	84(2)	585(16)	4(1)	3.6(1)	253(7)	1754(49)	6.0(2.0)	4.9(1)			
143	spo	0.9(2)	0.7(1)	4991(2002)	3.0(4)	20.9(3.0)	1.4(5)	1.35(7)	10(1)	70(10)	2.1(7)	1.9(1)	30(4)	209(30)	3.0(1.0)	2.6(1)			
144	spo	0.8(1)	1.7(1)	2677(263)	5.1(3)	35.1(2.1)	1.7(5)	1.57(5)	17(1)	117(7)	2.5(8)	2.2(1)	51(3)	351(21)	3.6(1.2)	3.1(1)			
145	spo	0.4(1)	0.7(1)	3030(507)	2.1(2)	14.5(1.2)	1.2(4)	1.22(4)	7(1)	48(4)	1.8(6)	1.7(1)	21(2)	145(12)	2.7(0.9)	2.4(1)			
147	spo	0.6(1)	0.8(1)	3430(605)	2.8(3)	19.5(1.9)	1.4(4)	1.33(5)	9(1)	65(6)	2.0(7)	1.9(1)	28(3)	195(19)	2.9(1.0)	2.6(1)			
148	spo	2.0(2)	3.5(1)	3587(323)	11.0(4)	76.4(3.0)	2.1(7)	1.97(6)	37(1)	255(10)	3(1)	2.8(1)	110(4)	764(30)	4.6(1.5)	3.8(1)			
151	spo	6.2(5)	11.9(4)	2763(192)	36(1)	250.9(8.6)	3(1)	2.78(8)	121(4)	836(29)	5(2)	3.9(1)	363(12)	2509(86)	6.8(2.2)	5.4(2)			
153	spo	0.9(1)	2.6(1)	2408(160)	7.0(3)	48.3(2.0)	1.8(6)	1.73(5)	23(1)	161(7)	2.7(9)	2.4(1)	70(3)	483(20)	3.9(1.3)	3.4(1)			
156	SDA	0.6(1)	0.7(1)	2788(365)	2.6(2)	3.1(2)	0.7(8)	1.37(6)	9(1)	10(1)	1.0(2)	1.9(1)	26(2)	31(2)	1.5(1.7)	2.7(1)			
157	SDA	1.5(1)	3.7(2)	2649(171)	10.4(4)	12.3(5)	1.1(5)	2.03(9)	35(1)	41(2)	1.6(8)	2.9(1)	104(4)	123(5)	2.3(2.7)	4.0(2)			
158	spo	0.6(1)	0.9(1)	2991(540)	3.1(3)	21.2(2.2)	1.4(5)	1.36(6)	10(1)	71(7)	2.1(7)	1.9(1)	31(3)	212(22)	3.0(1.0)	2.7(1)			
159	spo	1.3(2)	1.5(1)	3910(623)	5.6(4)	38.5(3.0)	1.7(6)	1.62(6)	19(1)	128(10)	2.5(8)	2.3(1)	56(4)	385(30)	3.7(1.2)	3.2(1)			
160	spo	0.7(1)	1.4(1)	4961(1518)	4.1(3)	28.3(2.2)	1.5(5)	1.48(5)	14(1)	94(7)	2.3(8)	2.1(1)	41(3)	283(22)	3.3(1.1)	2.9(1)			
161	spo	0.8(1)	0.6(1)	4967(1227)	2.8(3)	19.5(2.0)	1.4(4)	1.33(5)	9(1)	65(7)	2.0(7)	1.9(1)	28(3)	195(20)	2.9(1.0)	2.6(1)			
162	spo	1.3(1)	4.3(2)	2410(168)	11.1(4)	77.0(3.0)	2.2(7)	1.98(6)	37(1)	257(10)	3(1)	2.8(1)	111(4)	770(30)	4.6(1.5)	3.9(1)			
164	spo	0.4(1)	0.8(1)	2754(391)	2.5(2)	17.6(1.5)	1.3(4)	1.29(5)	8(1)	59(5)	2.0(6)	1.8(1)	25(2)	176(15)	2.8(0.9)	2.5(1)			
165	LYR	1.3(2)	5.9(2)	2370(184)	14.4(5)	12.0(4)	1.5(1)	1.86(4)	48(2)	40(1)	2.3(1)	2.6(1)	144(5)	120(4)	3.3(0.1)	3.6(1)			
166	spo	1.0(2)	1.4(1)	3038(460)	4.8(5)	33.0(3.1)	1.6(5)	1.55(6)	16(2)	110(10)	2.4(8)	2.2(1)	48(5)	330(31)	3.5(1.1)	3.0(1)			
167	spo	0.7(1)	0.7(1)	3971(926)	2.9(3)	19.8(2.2)	1.4(4)	1.33(6)	10(1)	66(7)	2.0(7)	1.9(1)	29(3)	198(22)	2.9(1.0)	2.6(1)			
168	spo	0.9(2)	2.0(1)	2788(365)	5.8(4)	40.1(2.7)	1.7(6)	1.64(6)	19(1)	134(9)	2.6(8)	2.3(1)	58(4)	401(27)	3.7(1.2)	3.2(1)			
169	spo	0.8(1)	1.3(1)	3863(596)	4.2(3)	29.1(1.8)	1.6(5)	1.49(5)	14(1)	97(6)	2.3(8)	2.1(1)	42(3)	291(18)	3.3(1.1)	2.9(1)			
171	spo	0.3(1)	0.5(1)	4457(1492)	1.7(2)	12.1(1.5)	1.2(4)	1.16(5)	6(1)	40(5)	1.7(6)	1.6(1)	17(2)	121(15)	2.5(0.8)	2.3(1)			
172	spo	7.0(4)	15.5(5)	2520(158)	45(1)	311.4(8.7)	3(1)	2.96(9)	150(4)	1038(29)	5.1(1.7)	4.2(1)	450(13)	3114(87)	7.3(2.4)	5.8(2)			
175	spo	0.4(1)	0.3(1)	5070(1586)	1.4(2)	9.4(1.1)	1.1(4)	1.07(5)	5(1)	31(4)	1.6(5)	1.5(1)	14(2)	94(11)	2.3(0.8)	2.1(1)			
176	spo	0.6(1)	1.1(1)	2497(385)	3.4(3)	23.4(2.4)	1.5(5)	1.40(6)	11(1)	78(8)	2.2(7)	2.0(1)	34(3)	234(24)	3.1(1.0)	2.7(1)			
177	spo	0.7(2)	1.7(1)	3746(1274)	4.8(5)	33.4(3.6)	1.6(5)	1.55(6)	16(2)	111(12)	2.4(8)	2.2(1)	48(5)	334(36)	3.5(1.2)	3.0(1)			

Table A.2 (cont'd)

ID	Stream	$\eta = 5 \times 10^{-3}$					$\eta = 1.5 \times 10^{-3}$					$\eta = 5 \times 10^{-4}$				
		LE_R ($\times 10^4$ J)	LE_I ($\times 10^4$ J)	T (K)	KE_p ($\times 10^6$ J)	m_p (g)	r_p (cm)	d_c (m)	KE_p ($\times 10^6$ J)	m_p (g)	r_p (cm)	d_c (m)	KE_p ($\times 10^6$ J)	m_p (g)	r_p (cm)	d_c (m)
179	SDA	0.5(1)	1.2(1)	4646(1967)	3.4(3)	4.1(4)	0.7(9)	1.47(7)	11(1)	14(1)	1.1(3)	2.1(1)	34(3)	41(4)	1.6(1.8)	2.9(1)
180	spo	2.5(4)	3.3(2)	5171(1433)	11.6(9)	80.1(6.4)	2.2(7)	2.00(7)	39(3)	267(21)	3(1)	2.8(1)	116(9)	801(64)	4.7(1.5)	3.9(1)
181	SDA	0.7(2)	1.2(1)	5634(2105)	3.8(4)	4.5(5)	0.8(9)	1.51(8)	13(1)	15(2)	1.1(3)	2.1(1)	38(4)	45(5)	1.6(1.9)	3.0(2)
182	spo	2.3(3)	7.4(2)	3022(349)	19.3(8)	133.6(5.9)	2.6(8)	2.32(7)	64(3)	445(20)	4(1)	3.3(1)	193(8)	1336(59)	5.5(1.8)	4.5(1)
183	spo	0.6(1)	0.6(1)	3791(726)	2.5(2)	17.5(1.7)	1.3(4)	1.29(5)	8(1)	58(6)	2.0(6)	1.8(1)	25(2)	175(17)	2.8(0.9)	2.5(1)
184	spo	3.5(3)	7.1(3)	3404(385)	21.2(8)	146.9(5.3)	2.7(9)	2.38(7)	71(3)	490(18)	4(1)	3.4(1)	212(8)	1469(53)	5.7(1.9)	4.6(1)
185	spo	1.3(3)	2.5(2)	3066(516)	7.6(6)	52.3(4.4)	1.9(6)	1.77(6)	25(2)	174(15)	2.8(9)	2.5(1)	76(6)	523(44)	4.1(1.3)	3.4(1)
186	spo	0.9(2)	1.6(1)	3248(528)	4.9(4)	33.9(2.7)	1.6(5)	1.56(6)	16(1)	113(9)	2.4(8)	2.2(1)	49(4)	339(27)	3.5(1.2)	3.0(1)
188	spo	2.5(2)	5.3(1)	3261(322)	15.5(5)	107.6(3.5)	2.4(8)	2.18(6)	52(2)	359(12)	4(1)	3.1(1)	155(5)	1076(35)	5.1(1.7)	4.2(1)
189	spo	0.6(2)	1.8(1)	1953(252)	4.7(4)	32.8(3.0)	1.6(5)	1.54(6)	16(1)	109(10)	2.4(8)	2.2(1)	47(4)	328(30)	3.5(1.1)	3.0(1)
191	spo	3.4(4)	9.5(3)	2635(265)	26(1)	178.1(7.1)	2.8(9)	2.52(8)	86(3)	594(24)	4(1)	3.6(1)	257(10)	1781(71)	6.1(2.0)	4.9(1)
192	spo	1.5(2)	2.6(2)	2600(232)	8.2(5)	56.9(3.7)	1.9(6)	1.81(6)	27(2)	190(12)	3(1)	2.6(1)	82(5)	569(37)	4.2(1.4)	3.5(1)
195	spo	7.2(6)	16.4(5)	2666(192)	47.3(1.5)	327.1(10.5)	3.5(1.1)	3.01(9)	158(5)	1090(35)	5(2)	4.3(1)	473(15)	3271(105)	7.4(2.5)	5.9(2)
199	spo	1.4(3)	3.4(2)	3081(624)	9.5(8)	65.4(5.4)	2.0(7)	1.89(7)	32(3)	218(18)	3(1)	2.7(1)	95(8)	654(54)	4.4(1.4)	3.7(1)
200	spo	0.7(2)	0.8(1)	3326(1077)	3.1(5)	21.2(3.7)	1.4(5)	1.36(8)	10(2)	71(12)	2.1(7)	1.9(1)	31(5)	212(37)	3.0(1.0)	2.7(2)
201	spo	0.8(2)	0.7(1)	4477(1909)	2.8(5)	19.6(3.2)	1.4(5)	1.33(7)	9(2)	65(11)	2.0(7)	1.9(1)	28(5)	196(32)	2.9(1.0)	2.6(1)
202	spo	2.4(3)	7.4(3)	2409(207)	19.8(9)	136.8(6.1)	2.6(9)	2.34(7)	66(3)	456(20)	4(1)	3.3(1)	198(9)	1368(61)	5.6(1.8)	4.6(1)
204	spo	0.8(2)	2.0(1)	2788(425)	5.6(4)	39.0(2.6)	1.7(6)	1.62(6)	19(1)	130(9)	2.6(8)	2.3(1)	56(4)	390(26)	3.7(1.2)	3.2(1)
205	spo	0.6(2)	1.5(1)	3297(993)	4.2(5)	29.3(3.1)	1.6(5)	1.49(6)	14(2)	98(10)	2.3(8)	2.1(1)	42(5)	293(31)	3.3(1.1)	2.9(1)
206	spo	1.3(4)	10.7(5)	2056(257)	24(1)	166.5(8.0)	2.8(9)	2.47(8)	80(4)	555(27)	4(1)	3.5(1)	241(12)	1665(80)	5.9(2.0)	4.8(1)
208	SDA	0.8(2)	1.3(2)	2744(516)	4.3(6)	5.1(7)	0.8(9)	1.57(9)	14(2)	17(2)	1.2(4)	2.2(1)	43(6)	51(7)	1.7(2.0)	3.1(2)
209	SDA	2.6(3)	7.2(5)	2435(410)	20(1)	23.4(1.3)	1.3(1.5)	2.45(11)	66(4)	78(4)	2(1)	3.5(2)	197(11)	234(13)	2.8(3.3)	4.8(2)
212	SDA	0.9(1)	2.7(1)	2575(204)	7.2(3)	8.6(4)	1.0(1.1)	1.83(8)	24(1)	29(4)	1.4(6)	2.6(1)	72(3)	86(4)	2.0(2.4)	3.6(2)
214	SDA	1.4(2)	4.9(4)	2271(242)	12.6(9)	15.0(1.1)	1.1(1.3)	2.15(10)	42(3)	50(4)	1.7(5)	3.1(1)	126(9)	150(11)	2.4(2.8)	4.2(2)
219	spo	0.4(1)	3.5(3)	1543(186)	7.7(6)	53.3(4.3)	1.9(6)	1.78(6)	26(2)	178(14)	2.8(9)	2.5(1)	77(6)	533(43)	4.1(1.3)	3.5(1)
223	spo	3.2(3)	3.1(1)	7426(1907)	12.7(6)	88.1(4.4)	2.3(7)	2.06(6)	42(2)	294(15)	3(1)	2.9(1)	127(6)	881(44)	4.8(1.6)	4.0(1)
224	spo	14.6(4)	28.6(3)	2858(285)	86(1)	597.4(7.0)	4.2(1.4)	3.58(10)	288(3)	1991(23)	6(2)	5.1(1)	863(10)	5974(70)	9.1(3.0)	7.0(2)
227	ORI	1.8(1)	3.4(1)	5084(755)	10.4(3)	4.6(1)	1.1(1)	1.73(16)	35(1)	15(1)	1.6(2)	2.4(2)	104(3)	46(1)	2.3(0.3)	3.4(3)
230	ORI	0.6(1)	1.2(1)	4254(1213)	3.7(3)	1.6(1)	0.8(1)	1.28(12)	12(1)	5.4(4)	1.1(2)	1.8(2)	37(3)	16(1)	1.6(0.2)	2.5(2)
231	ORI	0.3(1)	0.3(1)	4285(1532)	1.2(2)	0.5(1)	0.5(1)	0.93(9)	4(1)	1.8(2)	0.8(1)	1.3(1)	12(2)	5(1)	1.1(0.2)	1.8(2)
232	ORI	0.5(1)	0.6(1)	3512(466)	2.1(2)	1.0(1)	0.6(1)	1.09(10)	7(1)	3.2(2)	0.9(1)	1.5(1)	21(2)	10(1)	1.4(0.2)	2.1(2)
233	ORI	0.4(1)	0.4(1)	3800(543)	1.6(1)	0.7(1)	0.6(1)	1.00(9)	5(1)	2.4(1)	0.9(1)	1.4(1)	16(1)	7(1)	1.2(0.2)	2.0(2)
234	ORI	1.2(1)	2.0(1)	3677(488)	6.4(3)	2.8(1)	0.9(1)	1.50(14)	21(1)	10(1)	1.4(2)	2.1(2)	64(3)	28(1)	1.9(0.3)	2.9(3)
235	spo	0.6(1)	1.5(1)	3778(935)	4.1(3)	28.2(2.0)	1.5(5)	1.48(5)	14(1)	94(7)	2.3(8)	2.1(1)	41(3)	282(20)	3.3(1.1)	2.9(1)
236	TAU	1.3(1)	6.8(4)	2382(279)	16.3(8)	41.7(2.0)	1.5(8)	2.36(4)	54(3)	139(7)	2(1)	3.4(1)	163(8)	417(20)	3.3(1.6)	4.6(1)
238	TAU	0.6(2)	0.7(1)	3711(1109)	2.6(4)	6.6(9)	0.8(4)	1.38(6)	9(1)	22(3)	1.2(6)	2.0(1)	26(4)	66(9)	1.8(0.9)	2.7(1)
240	TAU	0.9(2)	2.2(1)	3005(472)	6.2(4)	15.7(1.1)	1.1(5)	1.78(4)	21(1)	52(4)	1.7(8)	2.5(1)	62(4)	157(11)	2.4(1.2)	3.5(1)
241	TAU	0.9(1)	2.3(1)	3080(453)	6.4(4)	16.3(1.0)	1.1(5)	1.80(4)	21(1)	54(3)	1.7(8)	2.6(1)	64(4)	163(10)	2.4(1.2)	3.5(1)
244	TAU	5.2(4)	9.4(3)	4475(883)	29(1)	74.0(2.5)	1.9(9)	2.79(4)	97(3)	247(8)	3(1)	4.0(1)	290(10)	740(25)	4.0(2.0)	5.4(1)
251	TAU	2.4(4)	8.1(4)	3065(517)	21(1)	54.0(2.8)	1.7(8)	2.55(5)	71(4)	180(9)	3(1)	3.6(1)	212(11)	540(28)	3.6(1.8)	5.0(1)
252	spo	2.2(3)	6.8(2)	3492(462)	18.0(7)	124.8(4.7)	2.5(8)	2.27(7)	60(2)	416(16)	4(1)	3.2(1)	180(7)	1248(47)	5.4(1.8)	4.4(1)
257	spo	1.7(2)	4.5(2)	2577(225)	12.3(5)	85.3(3.8)	2.2(7)	2.04(6)	41(2)	284(13)	3(1)	2.9(1)	123(5)	853(38)	4.8(1.6)	4.0(1)
259	spo	10.3(5)	23.3(7)	2579(197)	67(2)	465.1(12.0)	3.9(1.3)	3.33(10)	224(6)	1550(40)	66(2)	4.7(1)	672(17)	4651(120)	8.3(2.8)	6.5(2)
261	spo	0.5(1)	1.0(1)	4580(1240)	3.0(2)	20.5(1.4)	1.4(5)	1.35(5)	10(1)	68(5)	2.1(7)	1.9(1)	30(2)	205(14)	3.0(1.0)	2.6(1)
262	spo	0.9(2)	0.8(1)	4669(1310)	3.4(4)	23.4(2.7)	1.5(5)	1.40(6)	11(1)	78(9)	2.2(7)	2.0(1)	34(4)	234(27)	3.1(1.0)	2.7(1)

Table A.2 (cont'd)

ID	Stream	$\eta = 5 \times 10^{-3}$				$\eta = 1.5 \times 10^{-3}$				$\eta = 5 \times 10^{-4}$						
		LE_R ($\times 10^4$ J)	LE_1 ($\times 10^4$ J)	T (K)	KE_p ($\times 10^6$ J)	m_p (g)	r_p (cm)	d_c (m)	KE_p ($\times 10^6$ J)	m_p (g)	r_p (cm)	d_c (m)	KE_p ($\times 10^6$ J)	m_p (g)	r_p (cm)	d_c (m)
264	spo	1.3(2)	3.1(2)	2675(298)	8.7(5)	60.6(3.5)	2.0(7)	1.84(6)	29(2)	202(12)	3(1)	2.6(1)	87(5)	606(35)	4.3(1.4)	3.6(1)
266	spo	0.8(1)	2.0(2)	2856(307)	5.6(4)	38.9(2.5)	1.7(6)	1.62(5)	19(1)	130(8)	2.6(8)	2.3(1)	56(4)	389(25)	3.7(1.2)	3.2(1)
267	spo	0.6(1)	1.6(1)	3144(623)	4.4(4)	30.4(2.4)	1.6(5)	1.51(5)	15(1)	101(8)	2.4(8)	2.1(1)	44(4)	304(24)	3.4(1.1)	2.9(1)
268	spo	0.5(1)	0.3(1)	7336(2244)	1.5(2)	10.6(1.1)	1.1(4)	1.11(5)	5(1)	35(4)	1.7(5)	1.6(1)	15(2)	106(11)	2.4(0.8)	2.2(1)
269	spo	0.7(1)	2.7(1)	2745(381)	6.7(3)	46.3(2.3)	1.8(6)	1.71(5)	22(1)	154(8)	2.7(9)	2.4(1)	67(3)	463(23)	3.9(1.3)	3.3(1)
272	spo	0.8(1)	1.9(1)	3054(428)	5.4(3)	38(2)	1.7(6)	1.61(5)	18(1)	125(8)	2.5(8)	2.3(1)	54(3)	375(23)	3.6(1.2)	3.1(1)
275	LYR	0.4(1)	0.8(1)	3260(600)	2.5(2)	2.1(2)	0.9(1)	1.12(3)	8(1)	7(1)	1.3(1)	1.6(1)	25(2)	21(2)	1.8(0.1)	2.2(1)
276	spo	0.5(1)	0.9(1)	2597(485)	2.8(3)	19(2)	1.4(4)	1.32(6)	9(1)	64(7)	2.0(7)	1.9(1)	28(3)	191(22)	2.9(1.0)	2.6(1)
279	spo	1.1(2)	2.9(2)	2630(400)	8.0(6)	56(4)	1.9(6)	1.80(6)	27(2)	185(14)	2.9(9)	2.5(1)	80(6)	555(41)	4.1(1.4)	3.5(1)
280	spo	2.1(2)	3.9(2)	3860(681)	12.0(6)	83(4)	2.2(7)	2.02(6)	40(2)	277(14)	3.3(1.1)	2.9(1)	120(6)	830(41)	4.7(1.6)	3.9(1)
281	spo	13.9(2)	37.5(9)	2824(237)	103(2)	711(13)	4.5(1.5)	3.77(11)	342(6)	2370(43)	6.7(2.2)	5.3(2)	1027(19)	7111(129)	9.6(3.2)	7.3(2)
282	spo	3.3(4)	9.1(3)	2335(262)	25(1)	171(7)	2.8(9)	2.49(8)	82(3)	569(23)	4.2(1.4)	3.5(1)	247(10)	1706(70)	6.0(2.0)	4.9(1)
283	spo	11.6(7)	19.9(8)	2935(465)	63(2)	435(15)	3.8(1.3)	3.27(10)	210(7)	1451(50)	5.7(1.9)	4.6(1)	629(22)	4354(150)	8.2(2.7)	6.4(2)
284	spo	1.0(3)	2.9(2)	2376(469)	7.7(8)	53(5)	1.9(6)	1.78(7)	26(3)	177(18)	2.8(9)	2.5(1)	77(8)	531(54)	4.1(1.3)	3.5(1)
285	spo	1.7(1)	1.0(1)	7520(2682)	5.4(3)	37.2(1.8)	1.7(6)	1.60(5)	18(1)	124(6)	2.5(8)	2.3(1)	54(3)	372(18)	3.6(1.2)	3.1(1)
286	spo	0.3(1)	0.3(1)	3911(1643)	1.3(2)	9.0(1.4)	1.1(3)	1.06(6)	4(1)	30(5)	1.6(5)	1.5(1)	13(2)	90(14)	2.3(8)	2.1(1)
287	spo	1.2(1)	3.4(2)	2372(375)	9.3(4)	64.3(3.1)	2.0(7)	1.88(6)	31(1)	214(10)	3(1)	2.7(1)	93(4)	643(31)	4.3(1.4)	3.7(1)
289	spo	1.0(1)	2.4(1)	2905(316)	6.8(3)	47.1(2.4)	1.8(6)	1.71(5)	23(1)	157(8)	2.7(9)	2.4(1)	68(3)	471(24)	3.9(1.3)	3.3(1)
290	PER	0.2(1)	0.6(1)	2581(641)	1.7(2)	0.9(1)	0.6(1)	1.06(5)	6(1)	3(1)	0.8(1)	1.5(1)	17(2)	9(1)	1.2(1)	2.1(1)
292	spo	0.2(1)	0.4(1)	2326(791)	1.1(2)	7.6(1.6)	1.0(3)	1.01(7)	4(1)	25(5)	1.5(5)	1.4(1)	11(2)	76(16)	2.1(7)	2.0(1)
293	PER	0.5(1)	0.4(1)	4747(1153)	1.7(2)	0.9(1)	0.6(1)	1.07(5)	6(1)	3(1)	0.8(1)	1.5(1)	17(2)	9(1)	1.2(1)	2.1(1)
295	PER	1.5(1)	1.9(1)	4820(876)	6.8(4)	3.7(2)	0.9(1)	1.60(5)	23(1)	12(1)	1.3(1)	2.3(1)	68(4)	37(2)	1.9(2)	3.1(1)

Table A.3: Rough estimation of parameters of the suspected LIFs (based on the whole NELIOTA sample), projectiles and impact craters for $\eta = 1.5 \times 10^{-3}$. Errors are included in parentheses alongside values and correspond to the last digit(s).

ID	Stream	m_1 (mag)	$m_{R, est}$ (mag)	LE_1 ($\times 10^3$ J)	$LE_{R, est}$ ($\times 10^3$ J)	T_{est} (K)	$KE_{p, est}$ ($\times 10^6$ J)	$m_{p, est}$ (g)	$r_{p, est}$ (cm)	$d_{c, est}$ (m)
7	spo	10.9(3)	12.7(4)	1.5(5)	1.3(5)	2141(475)	1.9(3)	13(2)	1.2(4)	1.2(4)
8	spo	9.8(1)	11.7(3)	4.1(5)	3.1(9)	2012(276)	4.8(6)	33(4)	1.6(5)	1.6(5)
9	spo	9.6(1)	11.5(3)	5.0(5)	4(1)	1991(267)	5.7(7)	40(5)	1.7(6)	1.7(6)
10	spo	11.0(4)	12.7(4)	1.3(5)	1.2(5)	2158(510)	1.7(3)	12(2)	1.1(4)	1.2(4)
11	spo	11.0(4)	12.7(5)	1.4(5)	1.2(5)	2156(557)	1.7(3)	12(2)	1.1(4)	1.2(4)
15	SDA	9.3(1)	11.3(3)	6.7(7)	5(1)	1960(260)	7.6(9)	9(1)	1.0(5)	1.0(5)
25	spo	10.2(2)	12.1(4)	3.1(7)	2.4(8)	2061(360)	3.7(5)	26(4)	1.5(5)	1.5(5)
34	GEM	9.6(1)	11.6(3)	5.0(5)	4(1)	1990(261)	5.8(7)	9(1)	0.9(4)	0.9(5)
35	GEM	8.9(1)	10.7(3)	14(1)	9(3)	2163(321)	15(2)	23(3)	1.2(1)	1.2(6)
36	GEM	9.6(1)	11.5(3)	5.3(5)	4(1)	1985(261)	6.1(7)	9(1)	0.9(5)	0.9(5)
38	GEM	9.6(1)	11.5(3)	5.4(8)	4(1)	1984(281)	6.2(8)	10(1)	0.9(5)	0.9(6)
40	GEM	10.1(2)	12.0(3)	3.3(6)	2.6(8)	2054(331)	3.9(5)	6(1)	0.8(3)	0.8(3)
41	GEM	10.3(2)	12.1(3)	2.9(5)	2.3(7)	2069(316)	3.4(5)	5(1)	0.7(3)	0.8(3)
43	GEM	9.9(2)	11.7(3)	4.3(7)	3(1)	2006(292)	5.0(6)	8(1)	0.9(4)	0.9(5)
44	GEM	9.7(2)	11.6(3)	5.3(8)	4(1)	1985(285)	6.1(8)	9(1)	0.9(5)	0.9(5)
45	GEM	9.3(1)	11.2(3)	8(1)	5(2)	1949(268)	9(1)	13(2)	1.0(7)	1.0(7)
48	spo	9.6(1)	11.6(3)	5.6(7)	4(1)	1980(268)	6.4(8)	44(5)	1.8(6)	1.8(6)
57	spo	10.5(3)	12.3(4)	2.2(7)	1.8(7)	2098(433)	2.7(4)	19(3)	1.3(4)	1.4(4)
60	spo	9.8(2)	11.7(4)	4(1)	3(1)	2013(355)	4.8(7)	33(5)	1.6(5)	1.6(5)
77	spo	11.6(5)	13.2(5)	0.7(3)	0.7(3)	2232(718)	1.0(2)	7(2)	0.9(3)	1.0(3)
79	spo	9.7(1)	11.6(3)	5.1(9)	4(1)	1988(288)	5.9(8)	41(5)	1.7(6)	1.7(6)
80	spo	8.7(1)	10.7(3)	13.3(3)	8(2)	1894(233)	15(2)	100(11)	2.3(8)	2.3(8)
82	GEM	10.1(2)	12.0(3)	3.7(7)	2.8(9)	2043(324)	4.3(6)	7(1)	0.8(4)	0.8(4)
83	GEM	8.9(1)	11.0(3)	11(1)	7(2)	1914(256)	12(1)	18(2)	1.1(4)	1.1(6)
86	spo	9.0(2)	11.0(3)	10(1)	6(2)	1925(273)	11(1)	74(9)	2.1(7)	2.1(7)
87	spo	9.7(2)	11.6(3)	5.1(7)	4(1)	1990(283)	5.8(7)	40(5)	1.7(6)	1.7(6)
91	spo	9.6(2)	11.5(4)	5(1)	4(1)	1993(346)	5.7(8)	39(6)	1.7(6)	1.7(6)
92	spo	9.6(2)	11.5(4)	6(1)	4(1)	1974(331)	6.7(9)	47(6)	1.8(6)	1.8(6)
99	spo	9.5(2)	11.4(3)	6(1)	4(1)	1980(304)	6.3(8)	44(6)	1.8(6)	1.8(6)
113	SDA	9.8(2)	11.7(3)	4.1(6)	3.0(9)	2013(288)	4.7(6)	6(1)	0.8(9)	0.8(4)
123	spo	10.2(2)	12.0(3)	3.0(5)	2.3(7)	2066(328)	3.6(5)	25(3)	1.9(6)	1.5(5)
128	spo	10.8(2)	12.5(3)	1.6(3)	1.4(4)	2139(352)	2.0(3)	14(2)	1.5(5)	1.2(4)
129	spo	9.3(1)	10.7(3)	14(1)	9(3)	2548(447)	15(2)	102(11)	1.2(4)	2.4(8)
140	spo	9.6(1)	11.5(3)	5.9(6)	4(1)	1944(292)	6.7(8)	47(6)	2.3(8)	1.8(6)
141	spo	8.8(1)	10.9(3)	12(2)	8(2)	1906(257)	13(2)	90(11)	1.8(6)	2.3(7)
146	spo	10.0(1)	11.9(3)	3.9(5)	2.9(8)	2038(286)	4.5(6)	31(4)	2.2(7)	1.6(5)
150	spo	9.5(1)	10.8(3)	12.3(9)	8(2)	2679(502)	13(2)	93(10)	1.6(5)	2.3(8)
152	spo	9.8(1)	10.9(3)	9.4(6)	6(2)	2950(595)	10(1)	72(8)	2.6(9)	2.1(7)
154	SDA	9.6(1)	11.5(3)	4.8(6)	4(1)	1995(273)	5.6(7)	7(1)	2.3(7)	0.9(5)
155	SDA	9.4(1)	11.3(3)	5.9(6)	4(1)	1974(255)	6.8(8)	8(1)	2.1(7)	0.9(5)
163	spo	10.1(2)	11.3(3)	7(1)	5(2)	2920(626)	8(1)	58(7)	0.9(5)	2.0(6)
170	spo	9.6(1)	11.0(3)	9.6(9)	6(2)	2551(451)	11(1)	74(8)	0.9(5)	2.1(7)
173	spo	9.3(1)	10.6(3)	15(1)	10(3)	2632(484)	17(2)	115(13)	1.9(6)	2.5(8)
174	spo	9.8(2)	11.7(3)	4.8(8)	4(1)	1994(299)	5.6(7)	39(5)	2.1(7)	1.7(6)
187	spo	10.0(1)	11.3(3)	6.2(5)	4(1)	2743(523)	7.1(8)	49(6)	2.4(8)	1.9(6)
190	spo	9.6(1)	11.5(3)	5.2(7)	4(1)	1988(280)	5.9(7)	41(5)	1.7(6)	1.8(6)
193	ETA	7.4(1)	8.9(3)	98(3)	47(15)	2522(448)	96(10)	667(67)	1.8(6)	4(2)
194	spo	10.1(1)	12.0(3)	3.2(4)	2.5(7)	2059(286)	3.8(5)	27(3)	1.7(6)	1.5(5)
196	spo	9.2(1)	10.6(3)	16(1)	9.7(3)	2521(424)	17(2)	117(13)	4(1)	2.5(8)
197	spo	8.6(1)	10.7(3)	14(1)	8.9(3)	1888(235)	15(2)	107(12)	1.5(5)	2.4(8)
198	spo	9.4(1)	10.8(3)	13(1)	8.5(2)	2659(500)	15(2)	100(11)	2.5(8)	2.4(8)
207	SDA	9.9(1)	11.8(3)	4.2(4)	3.2(9)	2008(267)	4.9(6)	34(4)	2.4(8)	1.6(5)
210	SDA	8.7(1)	10.2(3)	22(1)	13(4)	2441(397)	24(3)	28(3)	2.3(8)	1.4(6)
211	SDA	9.4(1)	11.4(3)	6.2(8)	4(1)	1968(270)	7.1(9)	8(1)	1.6(5)	0.9(5)
213	SDA	10.0(2)	11.1(3)	8.2(8)	6(2)	3104(745)	9(1)	11(1)	1.4(6)	1.0(5)
215	SDA	8.0(1)	9.6(3)	39(3)	21(6)	2347(382)	40(4)	48(5)	0.9(5)	1.7(5)
216	SDA	9.4(2)	10.5(3)	15(2)	9(3)	2988(697)	16(2)	19(2)	1.0(5)	1.2(5)
217	spo	8.5(1)	9.9(3)	34(2)	19(6)	2531(440)	35(4)	42(4)	1.7(7)	1.6(5)

Table A.3 (cont'd)

ID	Stream	m_1 (mag)	$m_{R, est}$ (mag)	LE_1 ($\times 10^3$ J)	$LE_{R, est}$ ($\times 10^3$ J)	T_{est} (K)	$KE_{p, est}$ ($\times 10^6$ J)	$m_{p, est}$ (g)	$r_{p, est}$ (cm)	$d_{c, est}$ (m)
218	spo	9.9(3)	11.8(4)	5(1)	3.4(1)	2000(359)	5.3(8)	6(1)	1.2(5)	0.9(5)
220	spo	9.4(1)	11.3(3)	6.3(9)	4.4(1)	1968(276)	7.1(9)	49(6)	1.6(8)	1.9(6)
221	spo	8.4(1)	10.4(3)	16(2)	9.9(3)	1878(257)	17(2)	119(14)	0.8(4)	2.5(8)
222	ORI	9.9(2)	11.1(3)	9.5(8)	6.3(2)	2922(609)	11(1)	73(8)	1.8(6)	2.1(7)
225	spo	9.9(1)	11.8(3)	4.4(6)	3.3(9)	2005(279)	5.1(6)	35(4)	2.5(8)	1.7(5)
226	spo	9.1(1)	10.7(3)	13.5(8)	9(2)	2357(360)	15(2)	101(11)	2.1(7)	2.4(8)
228	ORI	9.8(1)	11.7(3)	4.6(6)	3(1)	2000(278)	5.3(6)	37(4)	1.6(5)	1.7(6)
229	ORI	8.9(1)	10.3(3)	20.6(9)	12(4)	2554(434)	22(2)	10(1)	2.3(8)	1.4(2)
237	TAU	7.7(1)	9.5(3)	43(4)	23(7)	2131(326)	44(5)	303(32)	1.7(5)	3(1)
239	TAU	10.2(2)	12.0(3)	2.9(6)	2.3(7)	2069(342)	3.5(5)	9(1)	1.4(2)	0.9(4)
242	TAU	9.0(1)	10.3(3)	17(1)	10(3)	2611(487)	18(2)	46(5)	3(1)	1.6(8)
243	TAU	9.4(2)	11.4(3)	5.7(8)	4(1)	1978(281)	6.5(8)	17(2)	0.9(4)	1.1(6)
245	TAU	9.0(1)	10.4(3)	16(1)	10(3)	2567(461)	18(2)	45(5)	1.6(8)	1.6(8)
246	TAU	9.5(2)	11.4(3)	5.4(9)	4(1)	1984(301)	6.2(8)	16(2)	1.1(5)	1.1(5)
247	TAU	9.0(2)	11.0(3)	8(1)	6(2)	1940(272)	9(1)	24(3)	1.6(8)	1.3(6)
248	TAU	9.5(2)	11.4(3)	5.2(9)	4(1)	1987(301)	6.0(8)	15(2)	1.1(5)	1.1(5)
249	TAU	8.9(1)	10.9(3)	9(1)	6(2)	1930(262)	10(1)	26(3)	1.3(6)	1.3(6)
250	TAU	9.4(2)	11.3(3)	6(1)	4(1)	1970(288)	7.0(9)	18(2)	1.1(5)	1.2(6)
253	spo	8.5(1)	10.0(3)	28(2)	16(5)	2475(418)	29(3)	74(8)	1.3(6)	1.9(9)
254	spo	9.5(1)	11.4(3)	6.1(8)	4(1)	1971(275)	6.9(8)	48(6)	1.2(6)	1.8(6)
255	spo	9.4(1)	11.4(3)	6.4(8)	5(1)	1966(270)	7.2(9)	50(6)	1.8(9)	1.9(6)
256	spo	8.8(1)	10.8(3)	12(1)	8(2)	1908(238)	13(1)	88(10)	1.8(6)	2.2(7)
258	spo	9.9(2)	11.8(3)	3.9(7)	3.0(9)	2016(320)	4.6(6)	32(4)	1.8(6)	1.6(5)
260	spo	10.4(2)	12.2(3)	2.2(4)	1.8(5)	2103(347)	2.6(4)	18(3)	2.2(7)	1.3(4)
265	spo	9.8(2)	11.7(3)	4.0(6)	3.0(9)	2014(297)	4.7(6)	32(4)	1.6(5)	1.6(5)
270	spo	10.0(1)	11.3(3)	6.6(6)	5(1)	2714(513)	7.5(9)	52(6)	1.3(4)	1.9(6)
271	spo	10.2(1)	12.1(3)	2.9(4)	2.3(7)	2070(295)	3.4(4)	24(3)	1.6(5)	1.5(5)
273	spo	9.7(1)	11.6(3)	5.0(6)	4(1)	1990(265)	5.8(7)	40(5)	1.9(6)	1.7(6)
274	spo	8.7(1)	10.8(3)	12.3(9)	8(2)	1902(234)	13(2)	93(10)	1.4(5)	2.3(8)
277	LYR	9.7(1)	11.6(3)	5.1(7)	4(1)	1989(279)	5.9(7)	5(1)	1.7(6)	1.1(1)
278	LYR	10.1(2)	11.9(3)	3.6(6)	2.8(8)	2045(309)	4.3(6)	30(4)	2.3(7)	1.6(5)
288	spo	10.2(2)	12.1(3)	3.3(7)	2.6(8)	2055(337)	3.9(5)	27(4)	1.1(1)	1.5(5)
291	spo	9.3(1)	10.7(3)	13(1)	8(3)	2513(443)	14(2)	99(11)	1.5(5)	2.3(8)
294	spo	11.3(3)	13.0(4)	1.2(4)	1.1(4)	2170(486)	1.5(3)	11(2)	1.5(5)	1.1(4)

Table B.1: List of multiframe flashes after July 2019. Errors are included in parentheses alongside values and correspond to the last digit(s).

ID	Date & UT	m_R (mag)	m_I (mag)	T (K)	ID	Date & UT	m_R (mag)	m_I (mag)	T (K)
114i	2019 08 06 18:19:16.023	10.37(28)	8.71(12)	2237(317)	172iv			10.22(18)	
114ii			11.20(51)		172v			11.56(58)	
116i	2019 08 06 18:56:36.990	8.43(12)	7.38(7)	3151(305)	173i	2021 07 03 01:23:35.666		9.26(12)	
116ii			9.62(21)		173ii			10.37(26)	
118i	2019 08 26 02:50:56.348	10.65(27)	9.11(7)	2368(308)	177i	2021 07 16 18:49:32.113	9.96(34)	9.15(12)	3746(1274)
118ii			10.18(17)		177ii			9.77(25)	
124i	2019 09 23 03:36:21.556	10.20(28)	9.40(11)	3777(1042)	179i	2021 08 02 01:26:06.111	10.41(29)	9.85(14)	4646(1967)
124ii			10.39(32)		179ii			10.18(19)	
125i	2019 09 25 03:40:11.073	8.43(8)	7.42(5)	3212(207)	180i	2021 08 02 01:34:28.145	8.75(18)	8.28(9)	5171(1433)
125ii		10.75(26)	9.56(9)	2864(504)	180ii			10.02(36)	
125iii			11.05(26)		181i	2021 08 02 02:44:36.306	10.12(26)	9.72(15)	5634(2105)
126i	2019 10 22 04:11:36.271	10.00(18)	9.28(11)	4036(810)	181ii			10.37(20)	
126ii			10.89(40)		182i	2021 08 02 02:51:02.646	8.85(17)	7.74(6)	3022(349)
127i	2019 10 24 02:30:16.186	9.49(15)	7.88(7)	2288(160)	182ii			8.89(13)	
127ii			10.18(21)		182iii			9.81(27)	
129i	2019 11 02 16:20:44.065		9.26(12)		184i	2021 10 11 16:57:00.374	8.66(13)	7.73(8)	3404(385)
129ii			10.63(40)		184ii		10.79(35)	8.86(10)	1986(301)
130i	2019 11 02 17:19:19.668	10.22(29)	9.26(12)	3345(770)	184iii			9.69(16)	
130ii			10.86(40)		184iv			10.37(26)	
133i	2019 12 01 16:23:13.796	8.42(10)	5.57(7)	1438(53)	184e			10.83(32)	
133ii		11.17(41)	8.09(9)	1343(149)	185i	2021 10 12 16:31:15.618	9.33(22)	8.25(10)	3066(516)
133iii			9.15(17)		185ii			10.61(41)	
133iv			10.31(35)		186i	2021 10 12 17:42:17.599	9.75(20)	8.75(10)	3248(528)
136i	2019 12 20 04:34:16.679	9.50(20)	8.51(7)	3254(477)	186ii			11.09(41)	
136ii			9.59(17)		187i	2021 12 01 04:21:42.906		10.00(13)	
136iii			10.61(35)		187ii			11.26(36)	
138i	2020 01 30 17:18:08.539	11.03(33)	9.51(12)	2393(427)	188i	2021 12 08 16:15:10.805	8.58(12)	7.59(7)	3261(322)
138ii			10.06(19)		188ii			9.34(18)	
142i	2020 03 01 16:54:23.862	8.32(8)	7.15(4)	2919(161)	191i	2022 04 05 17:30:55.889	8.87(17)	7.53(6)	2635(265)
142ii			9.20(11)		191ii		9.55(22)	8.51(1)	3158(512)
142iii			10.13(20)		191iii			9.56(26)	
144i	2020 03 27 17:40:25.320	10.01(15)	8.70(8)	2677(263)	193i	2022 05 07 20:47:14.061		7.41(8)	
144ii			11.30(28)		193ii			8.05(10)	
145i	2020 03 29 18:14:10.875	10.83(23)	9.72(9)	3030(507)	195i	2022 06 03 18:21:31.378	7.96(11)	6.64(6)	2666(192)
145ii			11.87(36)		195ii		10.73(44)	8.43(7)	1725(270)
148i	2020 04 28 19:19:54.525	8.99(10)	8.13(5)	3587(323)	195iii			10.04(19)	
148ii			9.75(10)		195iv			10.04(19)	
150i	2020 06 16 02:09:14.848		9.53(13)		196i	2022 06 03 18:57:25.884		9.17(9)	
150ii			10.59(23)		196ii			10.58(25)	
151i	2020 06 25 18:28:18.340	7.92(7)	6.66(6)	2763(192)	198i	2022 06 03 19:34:16.804		10.55(23)	
151ii		10.86(41)	8.96(9)	2016(357)	198ii		9.44(13)	9.44(13)	
151iii			10.12(23)		199i	2022 06 04 18:20:50.612	9.40(28)	8.32(9)	3081(624)
151iv			10.85(40)		199ii			9.76(23)	
152i	2020 06 25 19:09:24.063		9.76(13)		202i	2022 06 23 01:46:07.604	8.73(15)	7.22(7)	2409(207)
152ii			11.02(35)		202ii			9.44(11)	
153i	2020 06 26 19:52:31.569	9.73(11)	8.22(7)	2408(160)	204i	2022 07 22 02:13:27.207	9.97(24)	8.73(7)	2788(425)
153ii			10.53(13)		204ii			10.45(22)	
157i	2020 07 26 19:10:25.428	9.15(10)	7.82(6)	2649(171)	205i	2022 07 22 02:48:11.224	10.27(36)	9.29(14)	3297(993)
157ii			10.15(19)		205ii			10.11(25)	
160i	2020 08 14 01:15:36.278	9.95(20)	9.45(12)	4967(1227)	206i	2022 07 22 02:49:51.365	9.36(29)	7.51(10)	2056(257)
160ii			10.26(23)		206ii			8.15(12)	
162i	2021 03 17 17:46:52.983	9.48(12)	7.97(6)	2410(168)	206iii			9.65(25)	
162ii			10.10(16)		206iv			10.30(44)	
162iii			11.16(35)		209i	2022 08 01 18:28:18.506	9.42(21)	7.62(13)	2103(230)
163i	2021 03 17 18:03:02.205		10.14(15)		209ii		10.45(28)	8.96(15)	2435(410)
163ii			11.04(57)		209iii			10.13(23)	
165i	2021 04 18 19:13:58.703	9.43(15)	7.89(6)	2370(184)	210i	2022 08 03 18:05:38.820		8.66(9)	
165ii			9.08(11)		210ii			10.16(23)	
165iii			10.55(25)		212i	2022 08 03 18:23:42.636	9.76(12)	8.37(8)	2575(204)
168i	2021 05 18 20:08:21.742	9.90(20)	8.66(7)	2788(365)	212ii			10.16(17)	
168ii			10.66(28)		213i	2022 08 03 19:02:12.594		10.04(19)	
169i	2021 06 15 19:06:12.914	9.96(15)	9.19(8)	3863(596)	213ii			10.59(27)	
169ii			10.94(25)		214i	2022 08 04 18:47:06.667	9.26(18)	7.63(13)	2271(242)
170i	2021 06 15 19:15:27.433		9.57(13)		214ii			9.71(33)	
170ii			11.11(48)		215i	2022 08 04 19:24:20.958		8.02(12)	
171i	2021 06 15 19:23:18.620	10.86(32)	10.19(16)	4457(1492)	215ii			9.55(18)	
171ii			10.70(26)		216i	2022 08 04 19:25:11.729		9.40(19)	
172i	2021 06 15 19:38:52.236	8.15(10)	6.73(6)	2520(158)	216ii			9.93(29)	
172ii		9.70(16)	8.33(8)	2595(250)	217i	2022 08 22 01:33:02.291		8.45(9)	
172iii			9.44(13)		217ii			9.48(19)	

Table B.1 (cont'd)

ID	Date & UT	m_R (mag)	m_I (mag)	T (K)	ID	Date & UT	m_R (mag)	m_I (mag)	T (K)
219i	2022 09 01 18:33:36.493	10.66(37)	8.04(14)	1543(186)	259iii		9.91(34)	7.78(10)	1839(244)
219ii			9.99(23)		259iv		10.56(56)	8.58(13)	1945(455)
222i	2022 10 19 01:43:11.699		9.88(15)		259v			9.24(17)	
222ii			10.68(26)		259vi			9.62(26)	
223i	2022 10 19 03:03:44.141	8.47(10)	8.25(6)	7426(1907)	261i	2022 12 26 16:48:14.320	10.26(20)	9.68(12)	4580(1240)
223ii			9.93(20)		261ii			10.37(20)	
223iii			10.75(37)		264i	2022 12 27 17:47:37.390	9.29(17)	7.98(9)	2675(298)
224i	2022 10 20 01:12:58.151	9.80(27)	7.94(8)	2053(245)	264ii			10.43(34)	
224ii		8.58(14)	7.38(8)	2858(285)	266i	2022 12 27 18:11:32.401	9.73(12)	8.53(13)	2856(307)
224iii		9.25(19)	7.94(8)	2680(321)	266ii			10.73(52)	
224iv		9.73(24)	8.51(10)	2829(446)	267i	2023 01 16 04:11:21.224	10.09(26)	9.04(9)	3144(623)
224v		10.04(26)	8.99(12)	3132(633)	267ii			10.34(26)	
224vi		10.36(33)	9.35(14)	3223(879)	269i	2023 02 22 17:52:04.312	9.97(19)	8.70(13)	2745(381)
224vii			9.70(19)		269ii			9.88(16)	
224viii			9.89(18)		269iii			10.59(23)	2991(540)
224ix			10.23(21)		270i	2023 02 24 17:25:21.560		10.00(13)	
224x			10.38(24)		270ii			11.30(34)	
224xi			10.45(28)		272i	2023 03 26 20:25:28.546	9.88(15)	8.79(5)	3054(428)
224xii			10.72(36)		272ii			10.72(23)	
224xiii			11.61(80)		275i	2023 04 23 18:04:39.828	10.60(18)	9.61(9)	3260(600)
226i	2022 10 20 02:05:55.914		9.14(9)		275ii			11.99(54)	
226ii			10.64(24)		279i	2023 04 24 20:02:42.098	9.6(2)	8.28(6)	2630(400)
227i	2022 10 20 02:56:37.878	9.08(10)	8.59(6)	5084(755)	279ii			10.43(32)	
227ii			10.48(20)		280i	2023 05 23 20:06:14.792	8.94(9)	8.16(3)	3860(681)
229i	2022 10 20 04:11:08.419		8.90(8)		280ii			9.62(15)	
229ii			10.08(16)		281i	2023 05 24 20:11:10.028	8.50(11)	7.28(8)	2824(237)
230i	2022 10 21 02:55:11.697	10.22(24)	9.56(10)	4254(1213)	281ii		8.32(11)	6.41(8)	2003(114)
230ii			12.44(98)		281iii		10.05(18)	8.11(8)	1980(167)
234i	2022 10 22 03:55:35.517	9.51(14)	8.68(7)	3677(488)	281iv		10.29(25)	8.96(9)	2511(365)
234ii			10.69(26)		281v			9.69(12)	
235i	2022 10 22 03:56:50.322	10.31(25)	9.51(11)	3778(935)	281vi			10.10(17)	
235ii			11.04(32)		281vii			10.40(22)	
236i	2022 10 29 17:03:58.478	9.25(19)	7.72(13)	2382(279)	281viii			10.76(30)	
236ii			8.72(14)		281ix			11.13(35)	
236iii			9.60(19)		281x			11.40(44)	
237i	2022 10 29 17:13:31.322		7.68(13)		282i	2023 05 24 21:03:20.168	9.10(18)	7.53(13)	2335(262)
237ii			9.96(24)		282ii		10.58(44)	8.78(14)	2102(427)
240i	2022 10 30 16:47:27.612	9.68(22)	8.56(9)	3005(472)	282iii			9.86(20)	
240ii			10.17(28)		282iv			10.79(32)	
241i	2022 10 30 16:54:54.929	9.65(19)	8.57(9)	3080(453)	283i	2023 05 25 20:34:27.999	7.51(10)	6.28(7)	2811(200)
241ii			9.87(18)		283ii		10.01(23)	8.86(9)	2935(465)
242i	2022 10 30 17:13:28.165		8.98(14)		283iii		10.83(46)	9.44(13)	2569(694)
242ii			10.11(29)		283iv			10.30(20)	
244i	2022 10 30 17:34:16.134	8.64(14)	8.03(11)	4475(883)	283v			10.64(29)	
244ii		9.36(19)	8.05(10)	2676(334)	283vi			11.40(53)	
244iii			9.01(13)		283vii			11.71(63)	
244iv			9.74(19)		284i	2023 05 26 18:17:43.624	9.79(37)	8.28(8)	2376(469)
245i	2022 10 30 17:41:51.409		8.98(13)		284ii			10.72(64)	
245ii			10.24(28)		287i	2023 06 22 20:03:20.188	10.18(20)	8.53(12)	2253(254)
251i	2022 10 31 19:17:17.423	8.60(21)	7.51(12)	3065(517)	287ii		10.51(28)	8.97(13)	2372(375)
251ii			9.19(22)		287iii			10.16(17)	
252i	2022 11 19 02:39:27.785	8.82(15)	7.92(8)	3492(462)	289i	2023 08 10 01:53:23.822	9.67(16)	8.50(6)	2905(316)
252ii			9.14(15)		289ii			10.44(28)	
253i	2022 11 19 02:45:43.608		8.51(10)		290i	2023 08 11 01:43:53.825	11.32(41)	9.94(14)	2581(641)
253ii			9.79(25)		290ii			12.29(77)	
257i	2022 12 18 03:37:48.471	9.11(14)	7.73(6)	2577(225)	291i	2023 08 11 02:53:30.790		9.28(13)	
257ii			9.98(19)		291ii			10.81(58)	
259i	2022 12 26 15:46:16.570	7.76(11)	6.38(8)	2579(197)	295i	2023 08 13 03:05:54.033	9.30(13)	8.76(8)	4820(876)
259ii		8.62(14)	6.67(8)	1969(131)	295ii			11.02(43)	

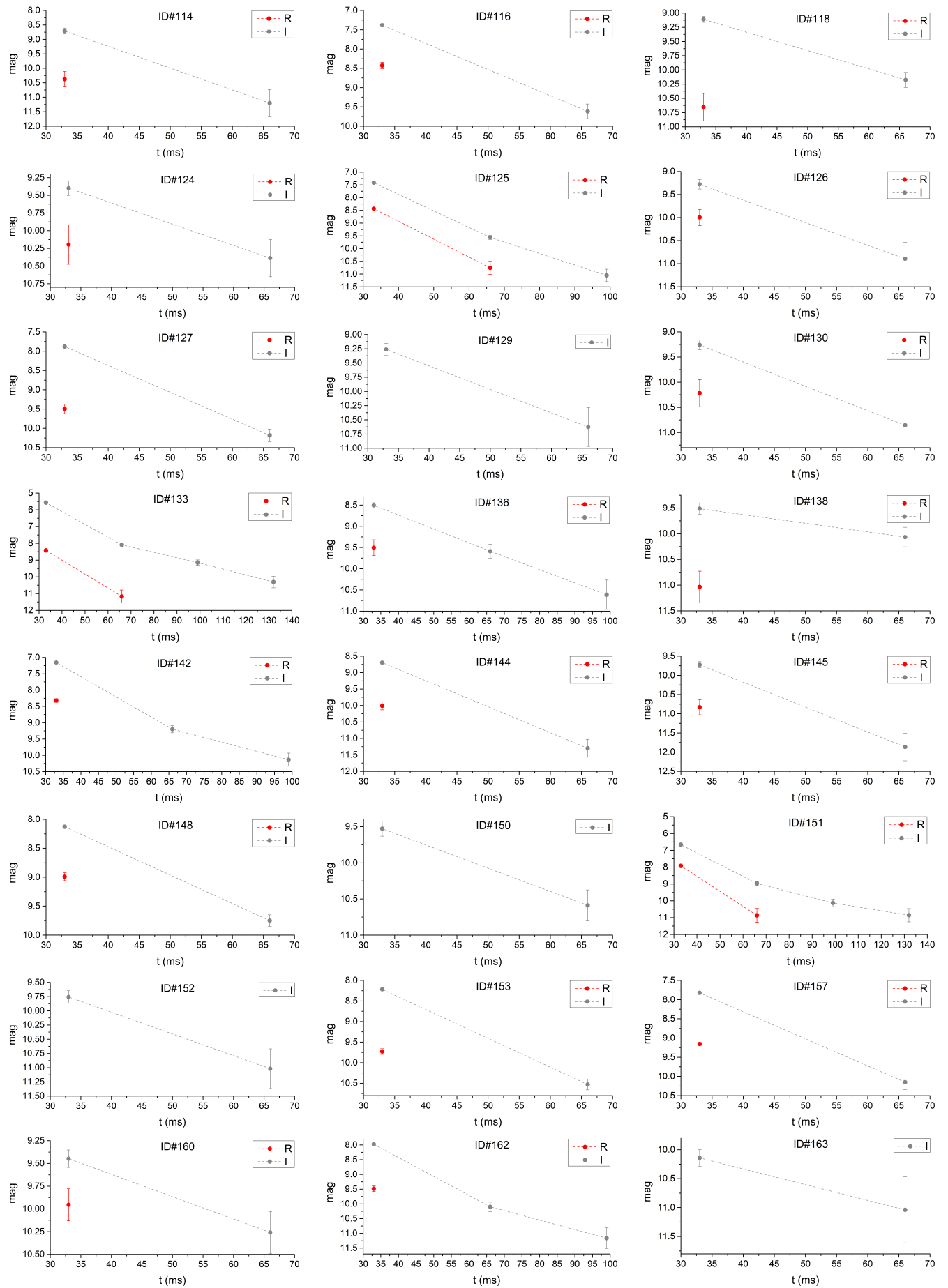


Fig. B.1: Light curves of the multiframe flashes.

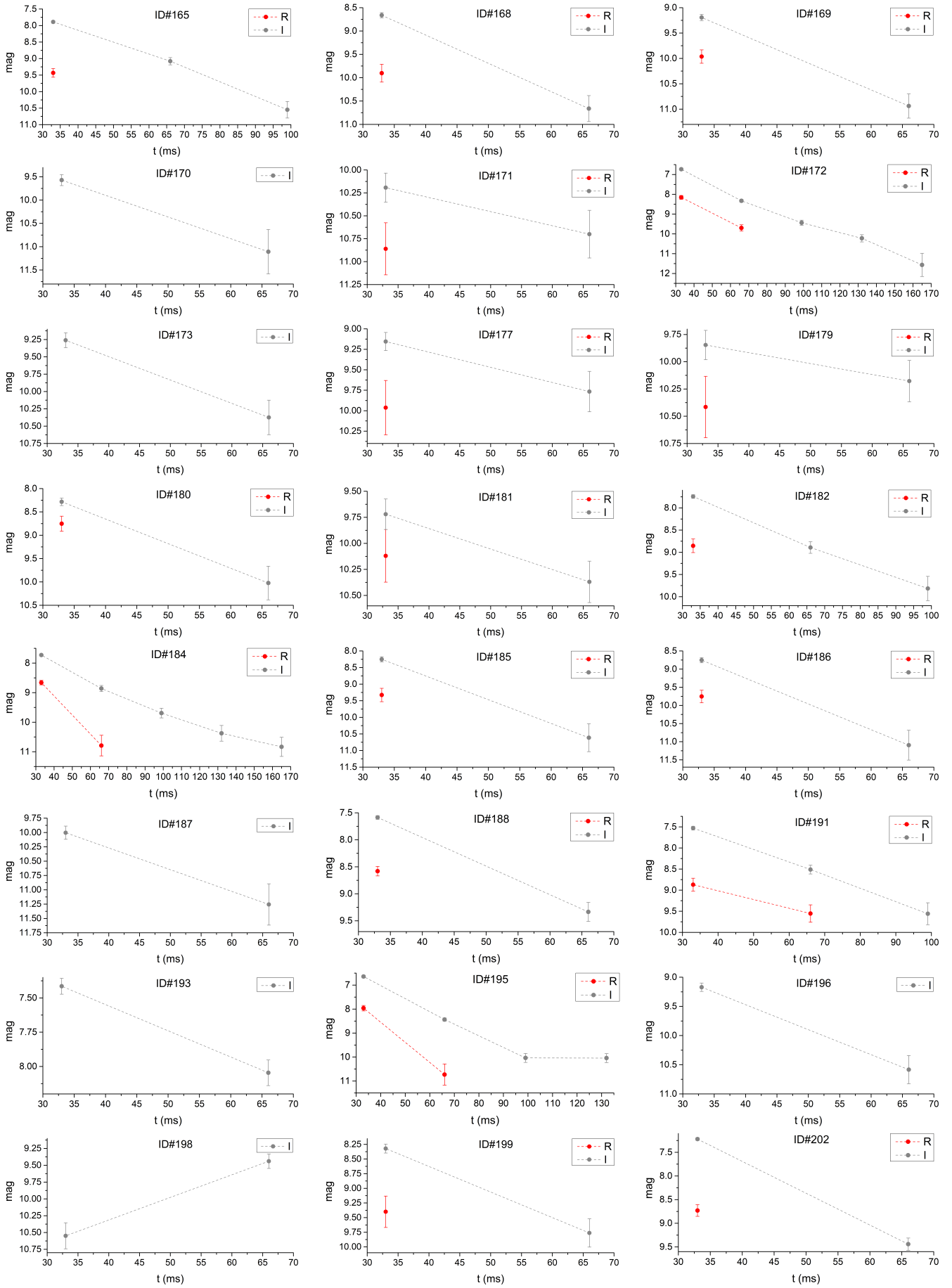


Fig. B.1 (cont'd)

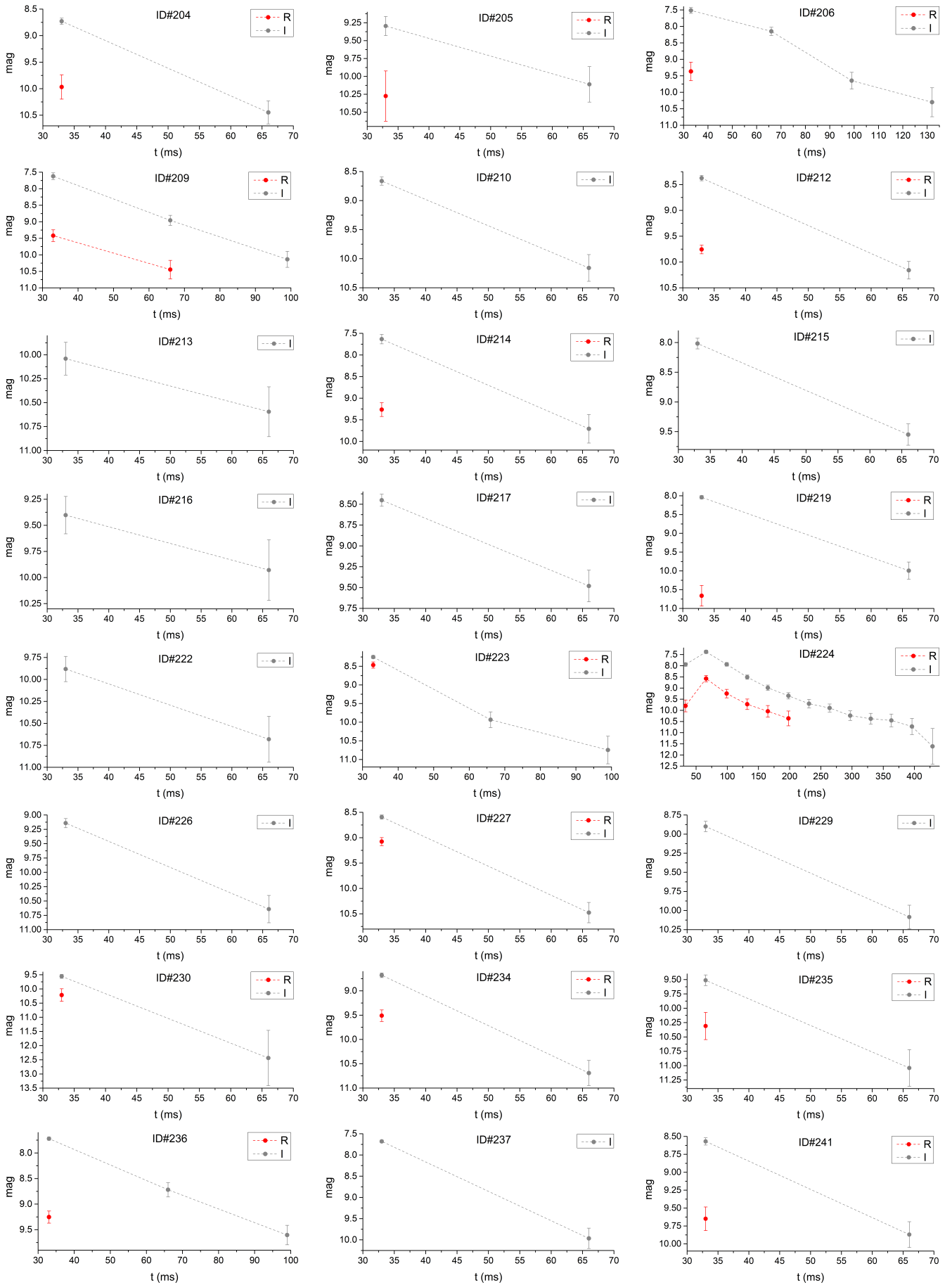


Fig. B.1 (cont'd)

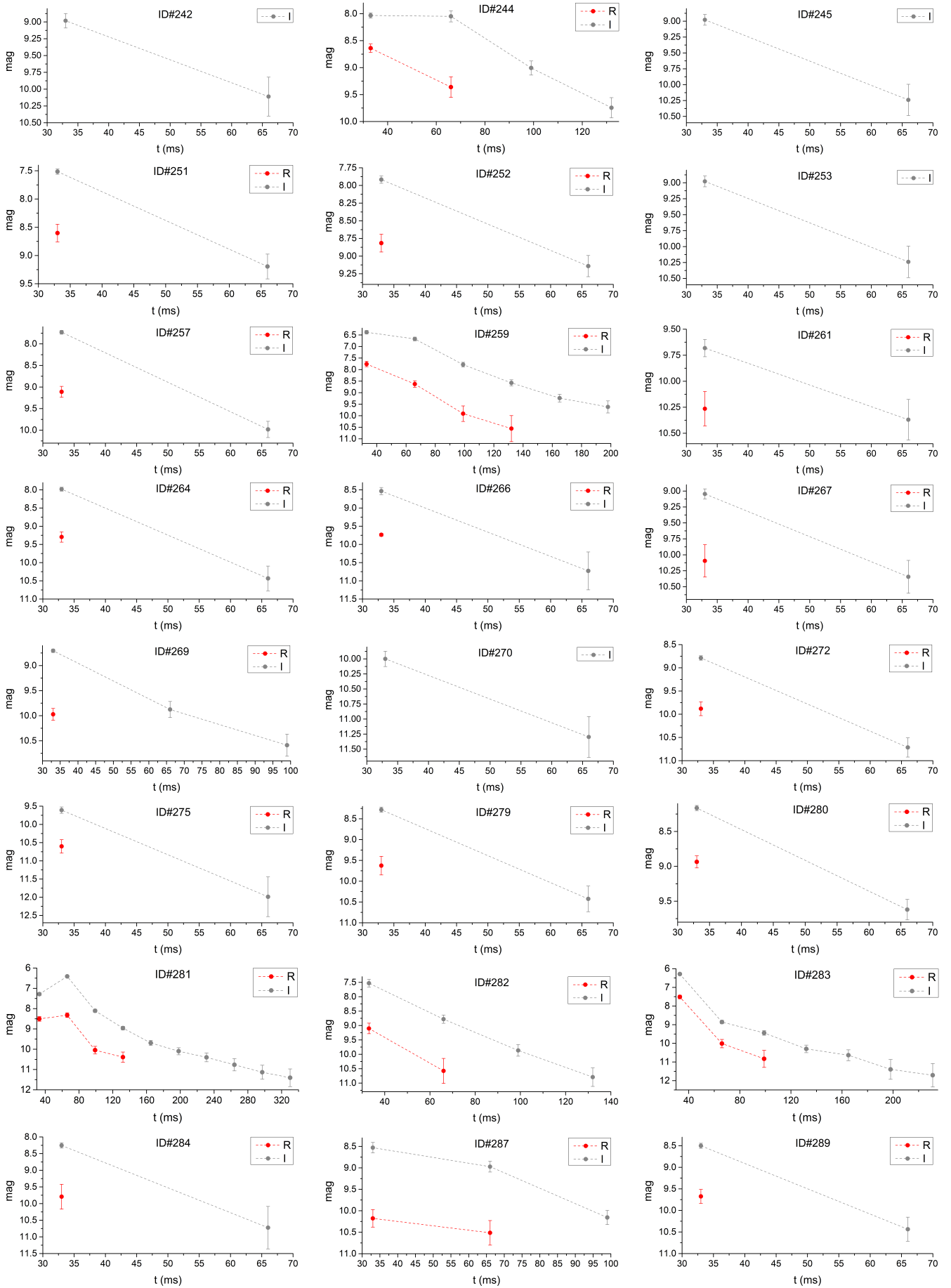


Fig. B.1 (cont'd)

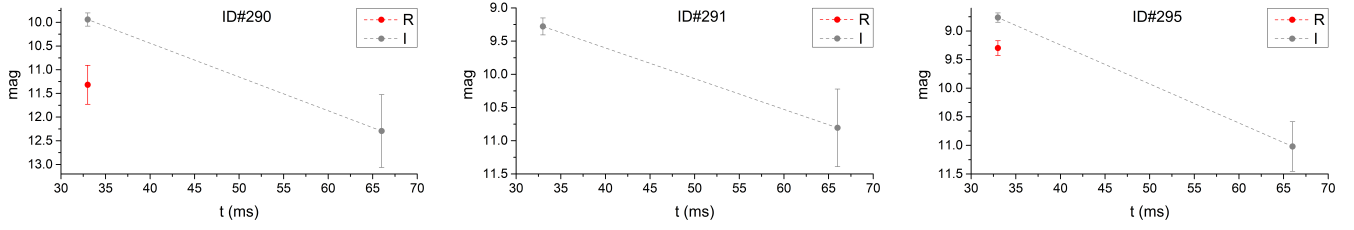


Fig. B.1 (cont'd)

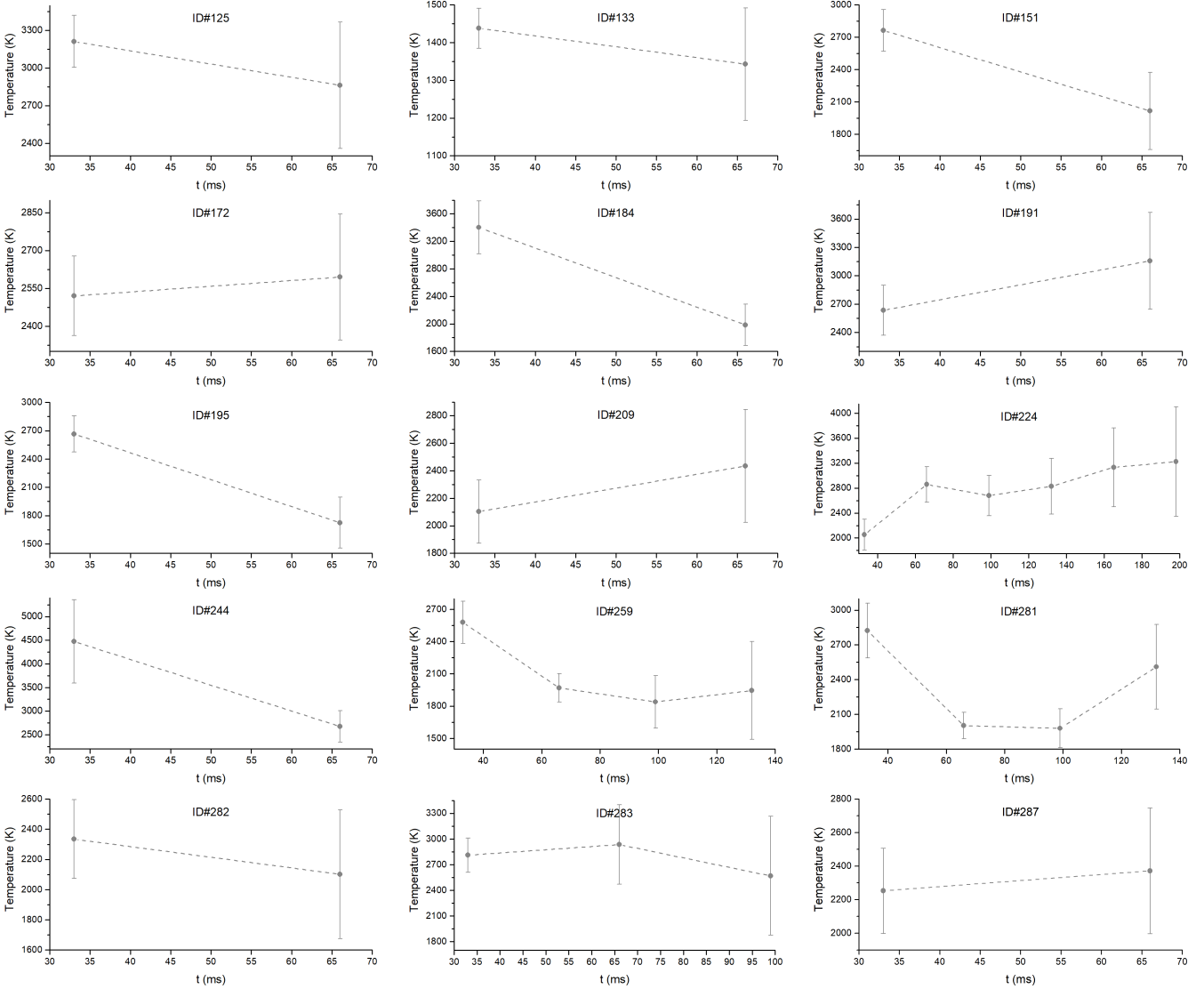


Fig. B.2: Temperature evolution curves of the multiframe flashes.

Table C.1: Parameters of sporadic and stream meteoroids.

CODE	$\lambda_{\odot,\text{beg}}$ ($^{\circ}$)	$\lambda_{\odot,\text{max}}$ ($^{\circ}$)	$\lambda_{\odot,\text{end}}$ ($^{\circ}$)	RA ($^{\circ}$)	Dec ($^{\circ}$)	l ($^{\circ}$)	b ($^{\circ}$)	V_p (km s^{-1})	$ZHR (max)$ (hr^{-1})	B (deg^{-1})	m_0 ($\times 10^{-7}$ kg)	s	r	ρ^a (g cm^{-3})
SPO								17			98.06	2.19	3	1.8(3)
Lyr	29.2	31.7	34.2	272	33	273	56.4	49	18	0.22	1.09	1.81	2.1	
ETA	27.3	45.8	64.3	338	-1	339.3	7.64	66	50	0.08	0.31	1.95	2.4	
Ari	57	76	95	45	23	49.15	5.71	38	30	0.1	3.21	2.12	2.8	
SDA	99.4	124.9	150.4	339	-17	334.2	-7.58	41	25	0.091	2.33	1.99	2.5	2.4(6)
Per	126.99	139.49	151.99	46	58	61.82	38.78	61	84	0.2	0.50	1.75	2	1.2(2)
Ori	192.9	207.9	222.9	95	16	94.84	-7.36	67	20	0.12	0.31	1.99	2.5	0.9(5)
Leo	230.4	234.4	238.4	153	22	147.06	10.15	71	23	0.39	0.24	1.92	2.33	0.4(1)
Gem	234.4	261.4	288.4	112	32	108.8	9.99	36	88	0.39	4.56	1.95	2.4	2.9(6)
QUA	253	283	313	231.5	48.5	203.3	63.3	41.7	120	1.8	2.33	2.30	1.9	1.9(2)
Urs	268.3	270.3	272.3	223	78	120.42	72.5	35	11.8	0.61	4.56	2.19	3	

Notes. ^ataken from Babadzhyanov & Kokhirova (2009)

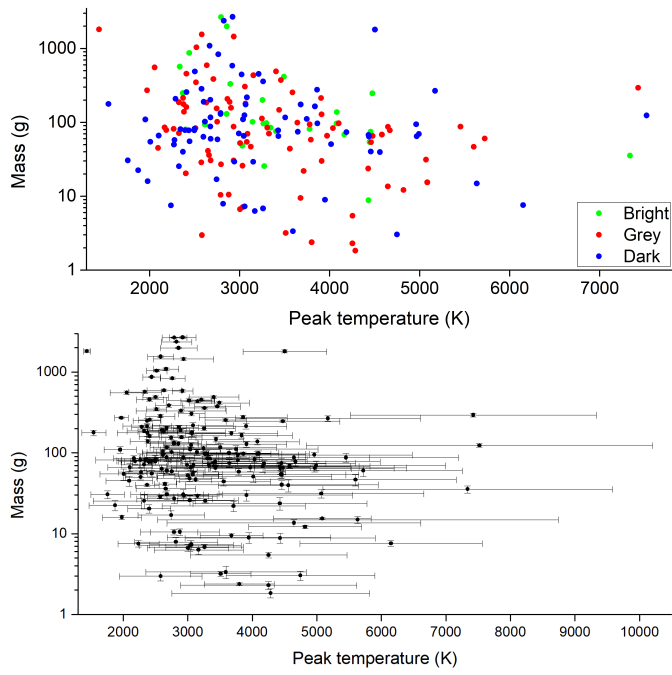


Fig. D.1: Correlation attempt of masses of meteoroids with the peak temperatures evolved during the impacts. Colors in the upper panel denote the rough characterization of the albedo of the local lunar soil where the impacts occurred. The lower panel is the same with the upper and contains the error bars.

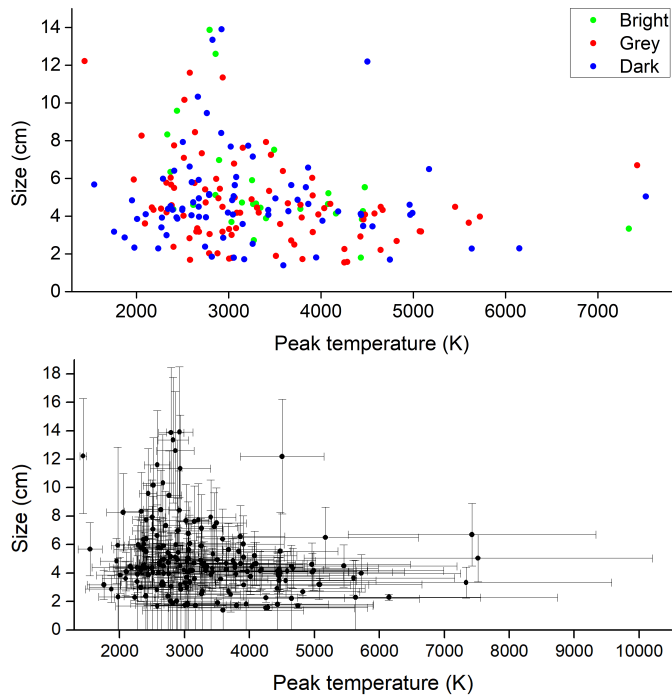


Fig. D.2: Correlation attempt of radii of meteoroids with the peak temperatures evolved during the impacts. Panels and symbols contain the same as in Fig. D.1.